Impact of Flue Gas Radiative Properties and Burner Geometry in Furnace Simulations

Yu Zhang and Feng Qian
Dept. of Automatic Control, Key Laboratory of Advanced Control and Optimization for Chemical Processes of Ministry of Education, East China University of Science and Technology, 130 Meilong Road, Shanghai 200237, China

Yu Zhang, Carl M. Schietekat, Kevin M. Van Geem, and Guy B. Marin
Dept. of Chemical Engineering and Technical Chemistry, Ghent University, Laboratory for Chemical Technology, Technologiepark 914, 9052 Gent, Belgium

DOI 10.1002/aic.14724
Published online January 19, 2015 in Wiley Online Library (wileyonlinelibrary.com)

Three fully coupled Computational Fluid Dynamics (CFD) simulations of a complete industrial steam cracking furnace equipped with floor burners are performed. The influence of the flue gas radiative properties and burner geometry on the flame front in the firebox, the heat transfer to the coils and the product selectivities has been investigated. A nine-band model developed from the Exponential Wide Band Model (EWBM) is used as nongray gas radiation model to compare with the gray gas implementation of Weighted Sum of Gray Gas Model for the evaluation of the flue gas radiative properties. The gray gas radiation model predicts a flue gas outlet temperature that is 70 K lower than the temperature obtained with the nongray gas radiation model, resulting in a 3.6% higher thermal efficiency and 44 K higher average Coil Outlet Temperature (COT). Important differences between the 22 reactors in the furnace are seen because of shadow effects with and without accounting for the detailed burner geometry. The maximum difference between the COT of different reactors in the furnace caused by shadow effects is about 29 K which corresponds to a propene-over-ethene difference of 0.1. Full furnace CFD simulations prove thus to be essential in design and during debottlenecking, when aiming for a more uniform COT distribution to the reactors by feed or fuel distribution. *AIChE J*, 61: 936–954, 2015
Keywords: steam cracking, computational fluid dynamics, heat transfer, gas radiative properties, shadow effect

Introduction

Steam cracking of hydrocarbons is the main petrochemical process for the production of light olefins, such as ethene and propene, which are key base chemicals for the chemical industry. The cracking chemistry mainly proceeds through a free-radical mechanism. As most reactions are highly endothermic, the process is carried out in tubular reactors with a high aspect ratio suspended in a large furnace. The energy required for heating of the process gas and the heat of reaction is supplied by combustion of a fuel from burners in the furnace floor and/or side walls. Downstream this so-called hot side, a complex separation section, that is, the cold side, separates the reactor effluent into the main product streams.

The process is very energy-intensive using about 8% of the chemical industry's primary energy consumption. Furthermore in naphtha steam crackers, about 65% of the total process energy is consumed by the hot side.[1] To improve the energy efficiency and the process selectivity, a lot of efforts have been made toward the development of detailed reaction networks describing the pyrolysis reactions,[2–5] which can be implemented into one-, two- or three-dimensional (3-D) reactor simulations.[6–10] The implementation of a coking model in these reactor simulations allows to predict run lengths.[11,12] Accurate results can be obtained by these reactor simulations, provided that the heat flux profile to the reactors is precisely defined. In other words, the quality of the reactor simulation depends on the accuracy of the simulation of the combustion and the heat transfer inside the furnace.

Over the past decades, significant progress has been made in the modeling of steam cracking furnaces. Coupled simulations of furnace and reactor coils were first performed using a combination of a computational fluid dynamics (CFD) model for the fluid dynamics and the Hottel's zone method[13] for the radiative heat transfer.[14,15] In this zone method, the computational domain is divided into several isothermal regions and the view factors between every two zones and surfaces are calculated. As the computational cost for the calculation of view factors increases exponentially with the number of zones, it is infeasible to use as many zones as are used in the fluid dynamics simulation. Hence, two different grids were used for the fluid dynamics and the radiative heat transfer calculation, with the former being much finer than the latter. With progress in radiation modeling and drastic

Correspondence concerning this article should be addressed to: F. Qian at fqian@ecust.edu.cn and K.M. Van Geem at Kevin.VanGeem@UGent.be.

increase in computational power, the Radiative Transfer Equation (RTE) can nowadays be solved in each cell of the flow domain to perform the fluid dynamics and radiative heat transfer calculation on the same grid. The six-flux radiation model was the first to be used,[16,17] followed by a comparison of several radiation models by Habibi et al.[18] More recently, a number of coupled furnace-reactor simulations of naphtha steam cracking furnaces were conducted using the commercial CFD software FLUENT.[19–23] Notwithstanding the great progress over the last decades in steam cracking furnace modeling, most of the reported previous works have three important shortcomings.

First of all, the flue gas radiative properties are typically described by the gray gas implementation of WSGGM, which is reported to yield unsatisfactory results in 3-D enclosures.[24] Moreover, as stated by Edwards, the "gray gas myth," shows that treating the flue gas as a gray gas in combustion systems may lead to temperature underpredictions of 100 K or more.[25] This was also confirmed by comparing gray and nongray gas models in steam cracking furnace simulations.[26,27] However, no coupled furnace-reactor simulations were performed in most of these works, which means that the influence on the product yields and coking rates of the radiative properties has not been evaluated. Furthermore, a uniform composition of the flue gas over the entire furnace was assumed in these works as the simulated furnaces only had radiation wall burners. However, the flue gas composition changes drastically in most steam cracking furnaces as floor burners or a combination of floor and wall burners is typically used. Hence, the effect of changing composition on the nongray gas model has to be considered.

Moreover, many reactors are suspended in a single furnace, with some closer to the burners and projecting shadows on other adjacent reactors reducing heat transfer to these reactors. This so-called "shadow effect"[28] causes nonuniformities in cracking severity over the different reactors and is not considered in most furnace-reactor simulations as only a single reactor is typically simulated.

Besides providing an accurate heat flux profile for reactor simulations, environmental concerns are another reason for the simulation of the fire side of steam cracking furnaces. The main pollutants from a furnace are carbon and nitrogen oxides. Detailed reaction networks result in high computational costs because of the vast number of species and reactions and the large grid size of the computational domain of the furnace. To save computational time, detailed reaction networks are often reduced before implementation in the furnace simulation[29,30] or the calculation of NO_x formation is performed in a postprocessing step.[31–33] It is well known that the details of the burner geometry, such as burner tips and stages, influence the formation of NO_x. Although these burner details are typically accounted for in the simulation of small test furnaces,[34] they are omitted in most industrial furnace simulations to reduce the grid size.[17,19] Therefore, the effect of simplifying the burner geometry in an industrial furnace simulation is assessed here.

In this work, three cases were studied for the investigation of the influence of flue gas radiative properties and burner geometry on the combustion and radiative heat transfer in an industrial naphtha cracking furnace equipped with floor burners. In all cases, shadow effects were evaluated by simulating all the reactors suspended in the furnace. A nine-band nongray gas model was developed from the Exponential Wide Band Model (EWBM) to compare with the gray gas implementation of the Weighted Sum of Gray Gasses Model (WSGGM). Two furnace configurations were established, one with the detailed burner geometry and the other with a simplified burner geometry. All simulations were performed using the commercial CFD software ANSYS FLUENT 14.0 with the nongray gas radiative properties model implemented in a User Defined Function (UDF). The reactor simulations were performed with COILSIM1D[7] developed in the Laboratory for Chemical Technology.

Reactor and Furnace Models

Reactor model

For a one-dimensional plug flow reactor, the species, momentum and energy transport equations form a set of ordinary differential equations

$$\frac{dF_i}{dz} = \frac{\pi d_i^2}{4} R_i \tag{1}$$

$$-\frac{dp}{dz} = \left(\frac{2f}{d_i} + \frac{\zeta}{\pi r_b}\right)\rho u^2 + \rho u \frac{du}{dz} \tag{2}$$

$$\sum_{i=1}^{N_s} F_i c_{p_i} \frac{dT}{dz} = \pi d_i q_i + \frac{\pi d^2}{4} \sum_{j=1}^{N_R} r_j \left(-\Delta H_j\right) \tag{3}$$

The first term at the right-hand side of Eq. (3) represents the heat flux to the reactors which is obtained from the furnace simulations. The second term accounts for the heat generation/consumption by the reactions. Based on the process gas temperature T_{gas} computed from Eq. (3), the internal TMT $T_{\text{w,i}}$ and external TMT $T_{\text{w,o}}$ can be calculated by the following equations

$$\mathrm{q}_i = h_{\text{c}} \left(T_{\text{w,i}} - T_{\text{gas}}\right) \tag{4}$$

$$\mathrm{q}_i = \frac{2\lambda_{\text{w}} \left(T_{\text{w,o}} - T_{\text{w,i}}\right)}{d_i \ln \frac{d_{\text{o}}}{d_i}} \tag{5}$$

where the convective heat transfer coefficient h_c is obtained from Dittus-Boelter correlation and λ_{w} is the thermal conductivity of the reactor tube alloy. This external TMT profile $T_{\text{w,o}}$ is then used in the furnace simulation.

The equations above are embodied in the COILSIM1D software package. An extensive reaction network with more than 750 components and thousands of elementary reactions is used to describe the gas-phase cracking chemistry.[35]

The detailed molecular composition of the feedstock is necessary because a boundary condition at the reactor inlet is needed for each species transport equation in the reactor simulation. For a complex feedstock like naphtha, only a limited number of so-called commercial indices are typically available such as specific density, average molecular mass, PIONA analysis, and so forth. Molecular reconstruction provides a detailed composition of the feedstock from these commercial indices.[36] The software package SimCO is adopted here. It uses the Shannon entropy maximization method or an Artificial Neutral Network (ANN) for naphtha's molecular reconstruction.[36,37]

Furnace model

Governing Equations. The mass, momentum and energy conservation equations for the flow of a 3-D, steady-state, compressible, reactive fluid are given by

$$\nabla \cdot \left(\rho \overrightarrow{u}\right) = 0 \tag{6}$$

$$\nabla \cdot \left(\rho \overrightarrow{u}\,\overrightarrow{u}\right) = -\nabla p + \nabla \cdot \left(\overline{\overline{\tau}}\right) + S_{\text{M}} \tag{7}$$

$$\nabla \cdot \left(\overrightarrow{u}(\rho E+p)\right)=\nabla \cdot \left(k_{\text{eff}}\nabla \text{T}-\sum_i h_i \overrightarrow{J}_i+\left(\overline{\overline{\tau}}_{\text{eff}} \cdot \overrightarrow{u}\right)\right)+S_{\text{E}} \tag{8}$$

where S_{M} is the source term of the momentum equation which includes the contributions due to any possible body forces. Only gravity is considered in the z-coordinate in this work, that is, $S_{\text{M},x}=S_{\text{M},y}=0$, $S_{\text{M},z}=-\rho g$. $\overrightarrow{J}_i$ in the energy governing equation represents the diffusive flux of species i. The source term in the energy equation S_{E} is the net volumetric heat release due to radiation and reactions.

Turbulence Model. The governing equations are transformed to the Reynolds Averaged Navier Stokes (RANS) equations. The Boussinesq hypothesis,[38] relating the Reynolds stresses to the mean velocity gradients is used to close the Reynolds stresses. The Renormalization Group (RNG) k-ε model[39] is adopted to calculate the turbulent viscosity by solving two additional transport equations for the turbulent kinetic energy k and its dissipation rate ε

$$\nabla \cdot \left(\rho \overrightarrow{u} k\right)=\nabla \cdot \left(\alpha_k(\mu+\mu_{\text{t}}) \cdot \nabla k\right)+P_k-\rho\varepsilon \tag{9}$$

$$\nabla \cdot \left(\rho \overrightarrow{u} \varepsilon\right)=\nabla \cdot \left(\alpha_\varepsilon(\mu+\mu_t) \cdot \nabla \varepsilon\right)+C_{1\varepsilon}\frac{\varepsilon}{k}P_k-C^*_{2\varepsilon}\rho\frac{\varepsilon^2}{k} \tag{10}$$

where $\mu_{\text{t}}=C_\mu \rho k^2/\varepsilon$ is the turbulent viscosity. $P_{\text{k}}=\mu_{\text{t}}S^2$ represents the production of turbulent kinetic energy, with S the modulus of the mean strain rate defined as $S_{ij}=\frac{1}{2}\left(\frac{\partial u_i}{\partial x_j}+\frac{\partial u_j}{\partial x_i}\right)$. $C^*_{2\varepsilon}=C_{2\varepsilon}+\frac{C_\mu \eta^3(1-\eta/\eta_0)}{1+\beta\eta^3}$, $\eta=Sk/\varepsilon$. α_k, $C_{1\varepsilon}$, $C_{2\varepsilon}$, C_μ, η_0, and β in the above-mentioned expressions are the model constants.

As the k-ε models are primarily valid for turbulent core flows and turbulent flows are significantly affected by the presence of a wall, it is important to represent the flow in the near wall region accurately. Two approaches of modeling near-wall region are provided, being wall functions and near-wall models. The large scale of the furnace leads to a drastic increase of the computational cost if a near-wall model is used. Furthermore, the influence of the reactor and furnace walls on the flow pattern in the furnace is limited due to the vast volume compared to the rather small wall surface area. Hence, the widely used standard wall function based on the work of Launder and Spalding[40] is adopted to account for the near-wall behavior.

This model deals with convective heat transfer on the reactor and refractory walls based on the Reynolds' analogy between momentum and energy transport, where the dimensionless temperature $T^*=\frac{\left(T_{\text{w}}-T_{\text{p}}\right)\rho c_{\text{p}}C_\mu^{1/4}k_{\text{p}}^{1/2}}{q_{\text{conv}}}$ and dimensionless distance from the wall $y^*=\frac{\rho y_{\text{p}}C_\mu^{1/4}k_{\text{p}}^{1/2}}{\mu}$ follow a linear relationship for the thermal conduction sublayer and a logarithmic law for the turbulent region. y_{p}, $T_{\text{p,}}$ and k_{p} represent the distance from the wall to the first near-wall node P, its temperature and its turbulence kinetic energy. All the expressions for heat transfer are well documented in the FLUENT user guide[41] and will not be duplicated here. As the reactor external wall temperature $T_{\text{w,o}}$ is imposed, the convective heat flux q_{conv} can be calculated.

Combustion Model. For a turbulent, non-premixed, combusting flow, the mole fraction Y_i of species i is calculated by solving the following species transport equations

$$\nabla \cdot \left(\frac{\overrightarrow{u}Y_i}{V_{\text{m}}}\right)=-\nabla \cdot \overrightarrow{J}_i+R_i \tag{11}$$

where V_{m} is the molar volume and R_i is the net rate of production of species i, given by the following sum over the N_{R} reactions in which species i participates

$$R_i=\sum_{j=1}^{N_{\text{R}}}\left(\upsilon''_{i,j}-\upsilon'_{i,j}\right)r_j \tag{12}$$

With $\upsilon''_{i,j}-\upsilon'_{i,j}$ the net stoichiometric coefficient of species i in reaction j and $r_{i,j}$ the reaction rate of reaction j. A simplified two-step global reaction network derived by Westbrook and Dryer[42] is used to describe the combustion process of the hydrocarbons. In this reaction network, hydrocarbons are converted to carbon monoxide and steam by partial oxidation in the first step. Carbon monoxide then reacts with oxygen to yield carbon dioxide

$$\text{CH}_4+1.5\text{O}_2 \rightarrow \text{CO}+2\text{H}_2\text{O} \tag{13}$$

$$\text{C}_2\text{H}_4+2\text{O}_2 \rightarrow 2\text{CO}+2\text{H}_2\text{O} \tag{14}$$

$$\text{CO}+0.5\text{O}_2 \rightarrow \text{CO}_2 \tag{15}$$

$$\text{H}_2+0.5\text{O}_2 \rightarrow \text{H}_2\text{O} \tag{16}$$

With the following reaction rate expressions

$$r_{\text{CH}_4}=1.5\times10^7 e^{-125580/RT}C_{\text{CH}_4}^{-0.3}C_{\text{O}_2}^{1.3} \tag{17}$$

$$r_{\text{C}_2\text{H}_4}=7.589\times10^7 e^{-125580/RT}C_{\text{C}_2\text{H}_4}^{0.1}C_{\text{O}_2}^{1.65} \tag{18}$$

$$r_{\text{CO}}=1.259\times10^{10} e^{-167430/RT}C_{\text{CO}}C_{\text{O}_2}^{0.25}C_{\text{H}_2\text{O}}^{0.5} \tag{19}$$

$$r_{\text{H}_2}=10^4 C_{\text{H}_2}C_{\text{O}_2}^{0.25} \tag{20}$$

For the combustion of hydrogen, the kinetic parameters in Eq. (20) are taken from Stefanidis et al.[17]

To account for the effect of turbulent mixing on the reaction rates, the Eddy-Dissipation Model (EDM) is adopted. The EDM, first developed by Magnussen and Hjertager,[43] assumes that the reactions taking place in the smallest turbulent structures are quite fast. Hence, the rate of combustion is determined by the rate of mixing of reactants contained in the molecular scale eddies, that is, the dissipation rate of the eddies. Consequently, the eddy dissipation rate, as well as the combustion rate, can be expressed to be proportional to the reciprocal of the eddy mixing time scale $\tau=k/\varepsilon$, leading to the following equations

$$R_{i,j}=\frac{\upsilon'_{i,j}}{V_m}A\frac{\varepsilon}{k}\min\left(\frac{Y_R}{\upsilon'_{R,j}}\right) \tag{21}$$

$$R_{i,j}=\frac{\upsilon'_{i,j}}{V_m}AB\frac{\varepsilon}{k}\frac{\sum_P Y_P}{\sum_P^N \upsilon''_{P,j}} \tag{22}$$

where A and B are empirical constants equal to 4.0 and 0.5, respectively. Equation. (21) represents the reaction rate calculated with the mole fraction of the limiting reactant involved in reaction j, while Eq. (22) is the rate limited by the presence of all the hot products. The net production of species i due to reaction j is then determined by the smaller of these two equations. EDM is adopted here in an extended form, introducing the Arrhenius reaction rate in Eq. (12) as a "switch" for the kinetically governed flame region.[44] This so-called finite-rate/EDM takes the minimum of the Arrhenius and eddy-dissipation reaction rates as the net reaction rate.

Radiation Model. The Discrete Ordinates (DO) model[45,46] is adopted to solve the RTE for a finite number of discrete solid angles, each associated with a vector direction $\vec{s}$, leading to the following equation

$$\nabla \cdot \left(I\left(\vec{r}, \vec{s}\right)\vec{s}\right) + (\kappa+\sigma_s) I\left(\vec{r}, \vec{s}\right) = \kappa n^2 \frac{\sigma T^4}{\pi} + \frac{\sigma_s}{4\pi} \int_0^{4\pi} I\left(\vec{r}, \vec{s}'\right) \Phi\left(\vec{s}, \vec{s}'\right) d\Omega' \tag{23}$$

The first term on the left-hand side represents radiative intensity changes along a path in direction $\vec{s}$. The decrease of intensity due to absorption and scattering away from direction $\vec{s}$ by the participating gases is modeled by the second term. On the right-hand side, the two terms account for the increase of intensity by emission from the hot gases and by the radiation scattered from other directions $\vec{s}'$ to $\vec{s}$, respectively.

FLUENT also provides a nongray implementation of the DO model solving the RTE for the spectral intensity I_i of each wavelength band separately, turning Eq. (23) into

$$\nabla \cdot \left(I_i\left(\vec{r}, \vec{s}\right)\vec{s}\right) + (\kappa_i+\sigma_s) I_i\left(\vec{r}, \vec{s}\right) = \kappa_i I_{b,i} + \frac{\sigma_s}{4\pi} \int_0^{4\pi} I_i\left(\vec{r}, \vec{s}'\right) \Phi\left(\vec{s}, \vec{s}'\right) d\Omega' \tag{24}$$

where κ_i is the spectral absorption coefficient. The refractive index n, scattering coefficient σ_s, and scattering phase function Φ are assumed to be wavelength independent. $I_{b,i}$ is the spectral black body intensity for the i-th band calculated by Planck's law

$$I_{b,i} = \left[f\left(n\lambda_{u,i}T\right) - f\left(n\lambda_{l,i}T\right)\right] n^2 \frac{\sigma T^4}{\pi \Delta\lambda_i} \tag{25}$$

where $\lambda_{u,i}$ and $\lambda_{l,i}$ are the upper and lower wavelength limits of the band, $\Delta\lambda_i = \lambda_{u,i} - \lambda_{l,i}$ is the width of band i, $f(n\lambda T)$ is the fractional emissive power of a black body and can be described as follows

$$f(n\lambda T) = \frac{15}{\pi^4} \sum_{m=1}^{\infty} \frac{e^{-m\zeta}}{m^4} \left[6 + 6(m\zeta) + 3(m\zeta)^2 + (m\zeta)^3\right], \quad \zeta = \frac{C_2}{n\lambda T} \tag{26}$$

where C_2 is the Planck constant. The total intensity over all bands is then calculated from

$$I\left(\vec{r}, \vec{s}\right) = \sum_i I_i\left(\vec{r}, \vec{s}\right) \Delta\lambda_i \tag{27}$$

Furnace refractory and reactor coils are always treated as opaque, diffuse walls when modeling the surface radiative heat transfer. In the case of gray gas radiation, the incident radiative heat flux on the wall is given by

$$q_{in} = \int_{\vec{s}\cdot\vec{n}>0} I_{in} \vec{s} \cdot \vec{n} d\Omega \tag{28}$$

The radiative heat flux leaving a surface is

$$q_{out} = (1-\varepsilon_w) q_{in} + n^2 \varepsilon_w \sigma T_w^4 \tag{29}$$

Where ε_w is the emissivity of the gray wall. Conversely, if the flue gas is considered as nongray, the radiative heat flux at the surface is calculated on the basis of each band using the following equations

$$q_{in,i} = \Delta\lambda_i \int_{\vec{s}\cdot\vec{n}>0} I_{in,i} \vec{s} \cdot \vec{n} d\Omega \tag{30}$$

$$q_{out,i} = \left(1-\varepsilon_{w,i}\right) q_{in,i} + \varepsilon_{w,i} \left[f\left(n\lambda_{u,i}T_w\right) - f\left(n\lambda_{l,i}T_w\right)\right] n^2 \sigma T_w^4 \tag{31}$$

where $\varepsilon_{w,i}$ is the wall emissivity within band i with an interval width $\Delta\lambda_i$. The net radiative wall heat flux q_{rad} is then calculated by $q_{rad} = q_{out} - q_{in}$ for gray gas radiation and $q_{rad} = \sum_i \left(q_{out,i} - q_{in,i}\right)$ for nongray gas radiation.

For most combustion processes in furnaces, the main absorbing gaseous species are H_2O, CO and CO_2 and scattering can be safely neglected ($\sigma_s = 0$).[47] In this case, the only unknown variable for solving the RTE is the absorption coefficient of the flue gas. Details in calculating the absorption coefficient are given in the next section.

Flue Gas Radiative Properties

Model selection

As mentioned before, solving the RTE for an absorbing-emitting gas mixture contained by opaque walls requires the knowledge of the gas radiative properties in terms of the absorption coefficient κ, which consists of millions of narrow spectral lines arising mainly from rotational and vibrational level transitions of the gas species of the mixture. To perform heat transfer calculations using these spectral lines, a great number of spectral evaluations of the RTE are required along with high resolution spectroscopic databases such as HITRAN and HITEMP.[48,49] These so-called Line-By-Line Radiative Transfer Models (LBLRTM) are computationally so expensive that even with today's powerful computing facilities, they can only be used as benchmarks for validation of more approximate models.

Spectral band models divide the wavelength spectrum into a number of spectral intervals in which the actual absorption coefficient is replaced by a smoothened average value. They can be further classified into narrow band models and wide band models based on the spectral resolution. Most of the narrow band models were developed about 60 years ago, among which there are two extremes in considering the overlapping of spectral lines. The Elsasser model assumes equally spaced lines of equal intensity, while the statistical model randomly distributes both line space and intensity.[50] The narrow band databases RADCAL[51] and EM2C,[52] established from spectroscopic measurements and the HITRAN database, respectively, are used in narrow band models to yield very accurate band transmittances and absorption coefficients.

Despite their high accuracy and efficiency, narrow band models still require too many bands to be used in the simulation of industrial furnaces as the grid size is too large, that is, in the order of millions of cells. As the blackbody intensity does not vary substantially across an entire vibration-rotation band, wide band models calculate the total absorption or emission for an entire band. The most successful wide band model is the EWBM proposed by Edwards and Balakrishnan.[53]

Gray gas modeling only calculates the total emissivity to solve the RTE over the entire spectrum as shown in Eq. (23). The most widely used model in this category is the

Weighted-Sum of Gray Gasses Model (WSGGM), first developed by Hottel and Sarofim within the framework of the zone method.[13] In this work, gray and nongray gas simulations based on WSGGM and EWBM respectively were used for the simulation of an industrial scale steam cracking furnace. In the next paragraphs, the model details and validation are given.

Weighted sum of gray gas model

This model replaces a nongray gas by a number of fictitious gray gases N, each of them having a constant absorption coefficient κ_i and a temperature dependent weight factor a_i. Hence, the total emissivity over a path length L can be expressed as

$$\varepsilon = \sum_{i=0}^{N} a_i(T)\left(1-e^{-\kappa_i L}\right) \tag{32}$$

As the total emissivity should have unity as limit as L tends to infinity, the sum of weight factors should also be unity. However, a single-component gas usually has spectral bands in which it would take a very large path length for the emissivity to be close to unity. To take this so-called spectral window into account, the absorption coefficient for the first fictitious gas $i=0$ is assigned to zero so the weight factor for $i=0$ is evaluated using the following expression making sure the total emissivity has unity as limit

$$a_0 = 1 - \sum_{i=1}^{N} a_i \tag{33}$$

It is common to approximate the temperature dependence of a_i by a polynomial

$$a_i = \sum_{j=1}^{M} b_{i,j} T^{j-1} \tag{34}$$

Values of $b_{i,j}$ and κ_i can be found by fitting Eq. (32) to the experimental total emissivity curve at different partial pressure ratios of the absorbing species, that is, H_2O and CO_2. The coefficients used in FLUENT are taken from Smith et al.[54] for the temperature range usually encountered in combustion applications, that is, between 600 and 2400 K and from Coppalle and Vervisch[55] for higher temperatures, both at a total pressure of 1 atm. Scaling rules suggested by Edwards and Matavosian[56] are used to correct κ_i in case of combustion under nonatmospheric pressure. However, it is important to note that WSGGM can also be applied in a nongray implementation by calculating an emissivity for each 'virtual' band using Eq. (32) per band. However, only a gray gas implementation of WSGGM is compatible with the radiation models in FLUENT.[41]

Exponential wide band model

The EWBM was developed based on the assumption that the line intensity decreases exponentially in the band wings far away from the band center. There are three types of wide band shapes according to the location of the band center, that is, bands with an upper limit head, bands with a lower limit head and symmetric bands. For each absorption band included in the EWBM, the band absorption coefficient κ is evaluated from Beer's law[27] with the band emissivity $\varepsilon = 1-\tau$

Table 1. Exponential Wide Band Correlation for an Isothermal Gas[50]

$\boldsymbol{\beta} \le 1$	$0 \le \tau_0 \le \boldsymbol{\beta}$	$\boldsymbol{A}^* = \tau_0$	Linear regime
	$\beta \le \tau_0 \le 1/\beta$	$A^* = 2\sqrt{\tau_0 \beta} - \beta$	Square root regime
	$1/\beta \le \tau_0 \le \infty$	$A^* = \ln(\tau_0 \beta) + 2 - \beta$	Logarithmic regime
$\boldsymbol{\beta} \ge 1$	$0 \le \tau_0 \le 1$	$A^* = \tau_0$	Linear regime
	$1 \le \tau_0 \le \infty$	$A^* = \ln\tau_0 + 1$	Logarithmic regime

$\tau_0 = \boldsymbol{\alpha X}/\boldsymbol{\omega}$ is the optical thickness at the band center, where $\boldsymbol{X} = \boldsymbol{\rho L}$ is the density path length.
$\boldsymbol{A}^* = \boldsymbol{A}/\boldsymbol{\omega}$ is the dimensionless band absorptance.

$$\kappa = \frac{1}{L}\ln\left(\frac{1}{1-\varepsilon}\right) \tag{35}$$

where τ is the band transmittance and is calculated by

$$\tau = \frac{\tau_0}{A^*}\frac{dA^*}{d\tau_0} \tag{36}$$

Edwards provided a four region expression[53] summarized in Table 1 to describe the dimensionless band absorptance A^* in Eq. (36) as function of the band strength parameter α, the line overlapping parameter β and the band width parameter ω. The temperature and pressure dependence of the parameters α, β, and ω are given below

$$\alpha(T) = \alpha_0 \frac{\Psi(T)}{\Psi(T_0)} \tag{37}$$

$$\beta(T) = \beta_0^* \sqrt{\frac{T_0}{T}}\frac{\Phi(T)}{\Phi(T_0)} P_e \tag{38}$$

$$\omega(T) = \omega_0 \sqrt{\frac{T}{T_0}} \tag{39}$$

$$P_e = \left[\frac{p}{p_0}\left(1+(b-1)\frac{p_i}{p}\right)\right]^n \tag{40}$$

Where α_0, β_0^*, and ω_0 are reference parameters, b and n are pressure parameters. The values of all parameters for the different species are taken from Modest.[50] $p_0 = 101325$ Pa and $T_0 = 100$ K are the reference pressure and temperature, respectively. The numerator and denominator of $\Psi(T)$ and $\Phi(T)$ consist of complicated series expressions which are rather computationally expensive. Lallemant and Weber[57] developed a more efficient method to calculate $\Psi(T)$ and $\Phi(T)$ using exact analytical expression and fourth-order polynomial correlations, respectively. They showed that the computational time for calculating the total emissivity of H_2O and CO_2 were 28 and 98 times faster by this approach with maximum relative errors less than 1% compared to calculation by Eqs. (37) and (38). Hence, the method of Lallemant and Weber[57] is adopted here.

For nongray implementation of the EWBM, the absorption coefficient should be determined for each wide band. First, the bandwidth is calculated using the following equation

$$\Delta\eta = \frac{A}{1-\tau} \tag{41}$$

τ can be described as a function of τ_0 and β by substituting the expressions in Table 1 into Eq. (36). However, the band transmittance will be equal to 1 in the linear regime of Table 1, which is usually encountered at very small path lengths, resulting in an infinite bandwidth. Therefore, Edwards suggested an upper limit of 0.9 for the calculation of band transmittance.[58] Ströhle and Coelho pointed out that an arbitrary

Table 2. Bands Information of the Nine-Band Model Derived from the EWBM

Band No.	Lower limit, (μm)	Upper limit, (μm)	Absorption coefficient, (m^{-1})
1	0	2.50	0
2	2.50	2.84	EWBM
3	2.84	4.15	0
4	4.15	4.69	EWBM
5	4.69	5.48	0
6	5.48	7.27	EWBM
7	7.27	12.42	0
8	12.42	18.92	EWBM
9	18.92	150.00	0

imposed upper limit may introduce serious errors if the recurrence relation is used due to a strong dependence on the grid resolution.[59] One way to remedy this is to define a fixed bandwidth $\Delta\eta_{\text{fix}}$ from the flue gas temperature and concentrations averaged over the entire domain first. Then the band limits can be determined using the following equations

$$\eta_u=\eta_c+\Delta\eta_{\text{fix}}/2 \quad \text{and} \quad \eta_l=\eta_c-\Delta\eta_{\text{fix}}/2 \tag{42}$$

$$\eta_u-\eta_l=\Delta\eta_{\text{fix}} \tag{43}$$

where $\eta=1/\lambda$ is the wavenumber which has the same units as the band absorptance. For a symmetric band, Eq. (42) is used to determine the upper and lower limits from a specified band center η_c. In the case of an asymmetric band, either the upper or the lower limit is known, so the other limit can be obtained by Eq. (43).

The band transmittance is then recalculated from the band absorptance A obtained from Table 1 by the following expression

$$\tau=1-\frac{A}{\Delta\eta_{\text{fix}}} \tag{44}$$

When calculating band transmittance for two overlapping bands, an effective band absorptance A_{eff} is used to replace the band absorptance A in Eq. (44) which can be calculated as[60]

$$A_{\text{eff}}=A_1+A_2-\frac{A_1}{\Delta\eta_1}\frac{A_2}{\Delta\eta_2}\Delta\eta_{\text{eff}} \tag{45}$$

where $\Delta\eta_{\text{eff}}$ is the effective bandwidth of the overlapping band, with its two limits chosen as the largest of the two overlapping bands' lower limits and the smallest of their upper limits.

Five absorption bands, two of which are overlapping and considered as one band, were suggested by Stefanidis et al.[27] for modeling the gas radiative properties in a steam cracking furnace, which has a similar flue gas composition as that of the present work. The centers of these bands are:

- H_2O: 6.3 and 2.7 μm
- CO_2: 15, 4.3, and 2.7 μm

Including the five spectral windows in-between the absorption bands, a nine-band model is developed using the EWBM as summarized in Table 2. The absorption coefficients of the spectral windows are set to zero. The averaged bandwidths over the temperature range from 300–2200 K are determined before the CFD simulation. The absorption coefficients are calculated on-the-fly, that is, as a function of temperature, pressure and H_2O and CO_2 concentrations in each cell during each iteration. To cover the entire wavelength spectrum with the nine-band model, the maximum wavelength, that is, the upper limit of the last band is computed as $\lambda_{\max}T_{\min}\geq 50,000$ as recommended by FLUENT,[41] where $T_{\min}$ is the minimum temperature in the furnace.

Model validation

Only five H_2O and CO_2 absorption bands, two of which are overlapping and considered as one band, out of the eleven included in the full EWBM are taken into account to limit computational time. Five spectral windows are present in-between the absorption bands, yielding a nine-band model. Because six absorption bands of full EWBM are omitted, the validity of the nine-band model under steam cracking furnace operating conditions needs to be verified. The total emissivities of H_2O and CO_2 calculated by the nine-band model and the full EWBM are compared with those calculated from a correlation developed by Leckner[61] based on spectrally integrated emissivities. For the nine-band model, the band energy approximation method[57] is adopted to evaluate the emissivity of each absorption band

$$\varepsilon_i=f(n\lambda_u T)-f(n\lambda_l T) \tag{46}$$

where the upper and lower band limits are computed by replacing the $\Delta\eta_{\text{fix}}$ in Eqs. (42) and (43) by band absorptance A. The emissivity of each species ε is then calculated by summing the emissivities of all bands.

Figure 1 shows the H_2O and CO_2 emissivities calculated by the nine-band model, the EWBM and Leckner's correlation for different path lengths at typical conditions in the furnace, that is, a total pressure of 101,325 Pa and a mole fraction of H_2O and CO_2 equal to 0.18 and 0.09, respectively. Figure 1a shows the results using a path length of 3 10^{-2} m, that is, the path length averaged over all cells of the computational domain. The path length of a cell is calculated as $L=3.6V/A$,[50] where V and A are the volume and the surface area of the cell, respectively. Good agreement between Leckner's correlation and EWBM is observed for both H_2O and CO_2 for most of the temperature range, but the errors tend to increase with increasing path length as shown in Figures 1b–d. This can mainly be attributed to the band absorptance increasing at larger path length, leading to more overlap of bands. As the way of dealing with overlapping bands in the EWBM is rather approximate, the emissivities calculated by the EWBM at larger path length are less accurate. However, it should be stressed that for the path length of the simulated furnace, that is, 3 10^{-2} m, the agreement between EWBM and Leckner's correlation is satisfactory.

Agreement between the EWBM and the nine-band model for CO_2 is excellent besides for the largest path length. The difference between the two models for H_2O is larger than for CO_2, especially at lower temperature and larger path lengths. The deviations are a result of omitting some absorption bands in the nine-band model compared to the full EWBM. To demonstrate this, the contribution of each band to the total emissivities of H_2O and CO_2 at a path length of 3 10^{-2} m is shown in Figure 2. The results at larger path lengths show similar trends and are therefore not depicted. Six bands of the EWBM are not included in the nine-band model, that is,71, 1.87, and 1.38 μm for H_2O; and 10.4, 9.4, and 2.0 μm for CO_2. The CO_2 bands at 10.4 and 9.4 μm contribute less than 0.1% to the total CO_2 emissivity at all temperatures used in Figure 1 and are therefore not depicted in Figure 2. The 2.0 μm band of CO_2 accounts for about 0.25% of the total CO_2 emissivity at a path length of 3 10^{-2} m. However, the contribution of the three omitted CO_2 bands increases

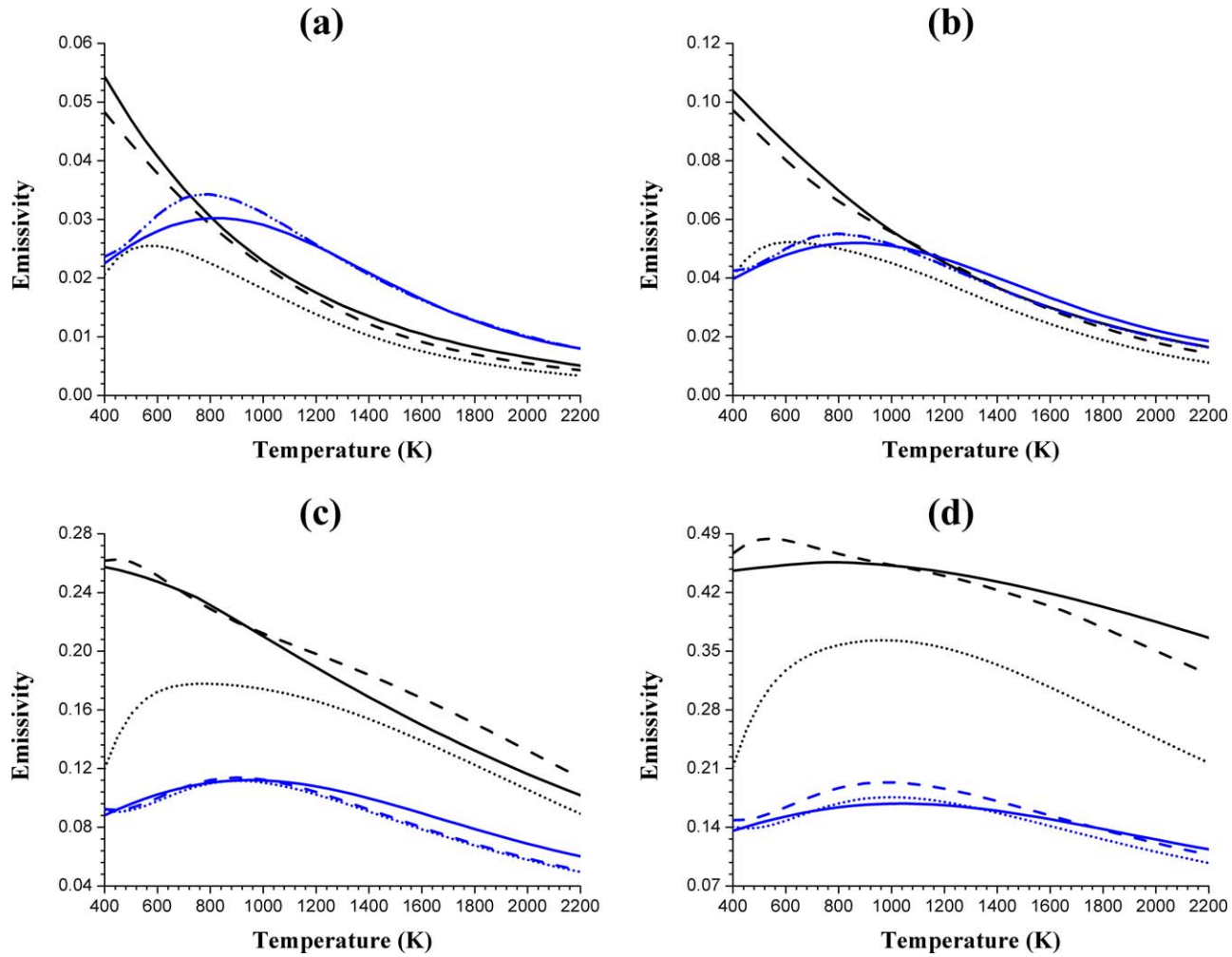

Figure 1. Emissivities of H_2O and CO_2 (——— – H_2O Leckner's; – – – – H_2O EWBM; ····· – H_2O nine-band model; ——— – CO_2 Leckner's; – – – – CO_2 EWBM; ····· – CO_2 nine-band model) as a function of temperature (K) at different path lengths L: (a) $L = 0.03$ m; (b) $L = 0.1$ m; (c) $L = 1$ m; (d) $L = 10$ m.

(Total pressure $p = 101325$ Pa; mole fraction $x_{H_2O} = 0.18, x_{CO_2} = 0.09$).

[Color figure can be viewed in the online issue, which is available at wileyonlinelibrary.com.]

with increasing path length and reaches a maximum value of 6% at 10 m, resulting in the underprediction of the total CO_2 emissivity by the nine-band model in Figure 1d. Hence, for large path length simulations, these bands could be important. The contribution of the omitted rotational band of H_2O at 71 μm to the total H_2O emissivity is almost 60% at 400 K but decreases rapidly with increasing temperature to about 10% at 2200 K. This band becomes less important when temperature is above 1200 K. The effect of the two excluded hot bands at 1.87 and 1.38 μm becomes more important at higher temperature. Consequently, the nine-band model underpredicts the H_2O emissivity at both low and high temperatures due to the omission of the rotational band and the hot bands, particularly for large path lengths, as shown in Figure 1.

For the path length used in the present furnace simulations, the nine-band model is only inaccurate at temperatures below 1200 K. However, H_2O and CO_2 are only formed at higher temperatures in the furnace. Hence, the effect of the inaccurate emissivity at lower temperatures on the simulation results is quite limited. This statement is corroborated by Figure 3, showing the average heat flux profile to all reactor coils in a small test furnace with a simplified coil geometry. Three simulations were performed using the gray implementation of the WSGGM, the nine-band model and the Leckner's correlation to calculate the gas radiative properties, respectively. The results using the nine-band model and the Leckner's correlation are almost identical. WSGGM predicts a more uniform heat flux profile because its emissivities were determined at a H_2O/CO_2 molar ratio of 0.5. Hence, it can be concluded that the nine-band model is suitable for the simulation of furnaces.

Simulation Methodology

Furnace geometry and operating conditions

The radiation section of an Ultraselective Conversion (USC) furnace was studied in the present work. Only one-fourth of the furnace, as depicted in Figure 4, was simulated to reduce the computational cost. Two sets of eleven U-coil reactors, are suspended in the center line of the furnace. Every U-coil has two passes, that is, an inlet and outlet leg connected by a return bend and a joint where the diameter gradually expands from the inlet leg diameter to the outlet leg diameter. Eight floor burners positioned against the furnace refractory side walls supply the heat for the endothermic cracking reactions. The burners are grouped in four sets of two burners at opposite sides of the reactors. Each burner has primary and staged fuel inlets

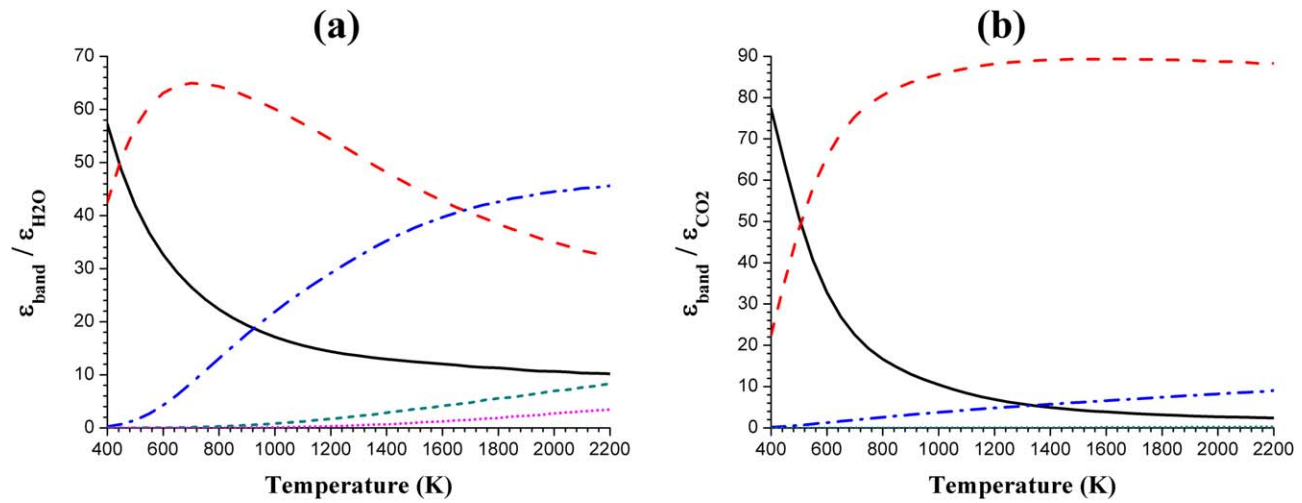

Figure 2. The ratio of band emissivity to the total emissivity (%) calculated using the EWBM as a function of temperature (K) at path length $L = 0.03$ m: (a) ——— – H_2O 71 μm band; – – – – H_2O 6.3 μm band (incl.); – • – – H_2O 2.7 μm band (incl.); – – – – H_2O 1.87 μm band; ····· – H_2O 1.38 μm band; (b) ——— – CO_2 15 μm band (incl.); – – – – CO_2 4.3 μm band (incl.); – • – – CO_2 2.7 μm band (incl.); ····· – CO_2 2.0 μm band.

(Total pressure $p = 101325$ Pa; mole fraction $x_{H_2O} = 0.18, x_{CO_2} = 0.09$; incl. indicates that the absorption band is included in the nine-band model). [Color figure can be viewed in the online issue, which is available at wileyonlinelibrary.com.]

reducing the non-premixed flame temperature and, hence the NO_x formation. The dimensions of the furnace and reactors, the fuel and feedstock composition and the operating conditions are summarized in Table 3.

Two furnace configurations were considered to investigate the effect of accounting for the burner details on the furnace simulation. In the first configuration, the geometrical details of the burners such as stages and tips were modeled, while in the second configuration the burners were modeled as a rectangular hole in the furnace floor as done in some previous work.[14,17] The fuel and air inlets in both configurations were extended upstream to ensure fully developed turbulent flow entering the furnace. A mixed meshing scheme was used to discretize the furnace domain. Hexahedral cells were used in the upper part of the furnace where the reactor tubes are straight. Tetrahedral cells were first generated near the burners and the return bends due to the geometrical complexity. The tetrahedral cells were then converted to polyhedral cells to reduce the number of cells and improve the numerical stability of the solver.[41] The mesh was refined until no significant changes of the flow variables at the furnace stack were simulated. The total number of cells of the furnace with detailed and simplified burners was about 6.39 and 7.24 million, respectively.

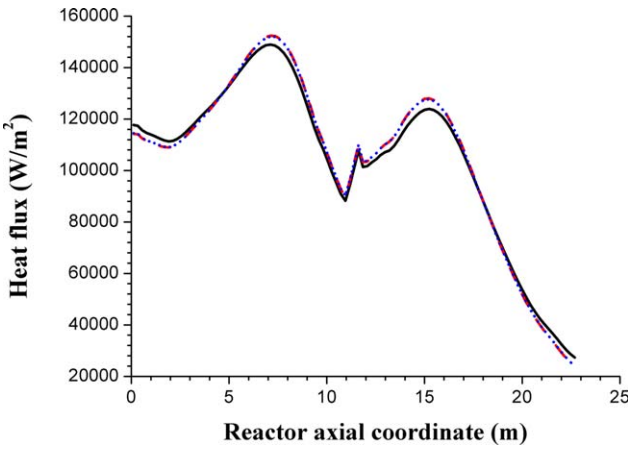

Figure 3. Averaged heat flux (W/m^2) over all reactors in the test furnace as a function of the reactor axial coordinate (m): ——— – WSGGM; – – – – Leckner's; ····· – nine-band model.

[Color figure can be viewed in the online issue, which is available at wileyonlinelibrary.com.]

Solution procedures

All the governing equations for the furnace simulation are discretized using the finite volume method and solved with a segregated solver. The convection operators are discretized by a second-order upwind scheme. The Semi-Implicit Method for Pressure-Linked Equations (SIMPLE) is used for pressure-velocity coupling. The commercial CFD software ANSYS FLUENT 14.0 is applied.

Three coupled furnace-reactor simulations were performed to evaluate the influence of flue gas radiative properties and burner geometry on the flow, combustion and heat transfer in the furnace. Gray and nongray gas radiation models were compared in the furnace configuration with detailed burner geometry. The default WSGGM implemented in FLUENT described above was used for the gray gas simulation as it was often used in previous work.[18–20,22,23] In the nongray simulations, the flue gas absorption coefficient was calculated by the above described nine-band model implemented in a user-defined function. The furnace refractory wall and reactor tubes were treated as gray diffusive walls in all three cases, in other words, the wall emissivity of all bands in the non-gray simulations is constant and specified in Table 3. The heat loss through the furnace refractory walls was calculated from a heat balance over the industrial unit and accounts for about 1% of the total heat of combustion. This value is set as a uniform heat flux boundary condition at the furnace walls.

The reason for performing coupled furnace-reactor simulations is to investigate the interaction between the fire side and process gas side for all three cases. Similar as in the work by Hu et al.,[20] solution procedure of the coupled simulation is described as follows. First a furnace simulation is performed

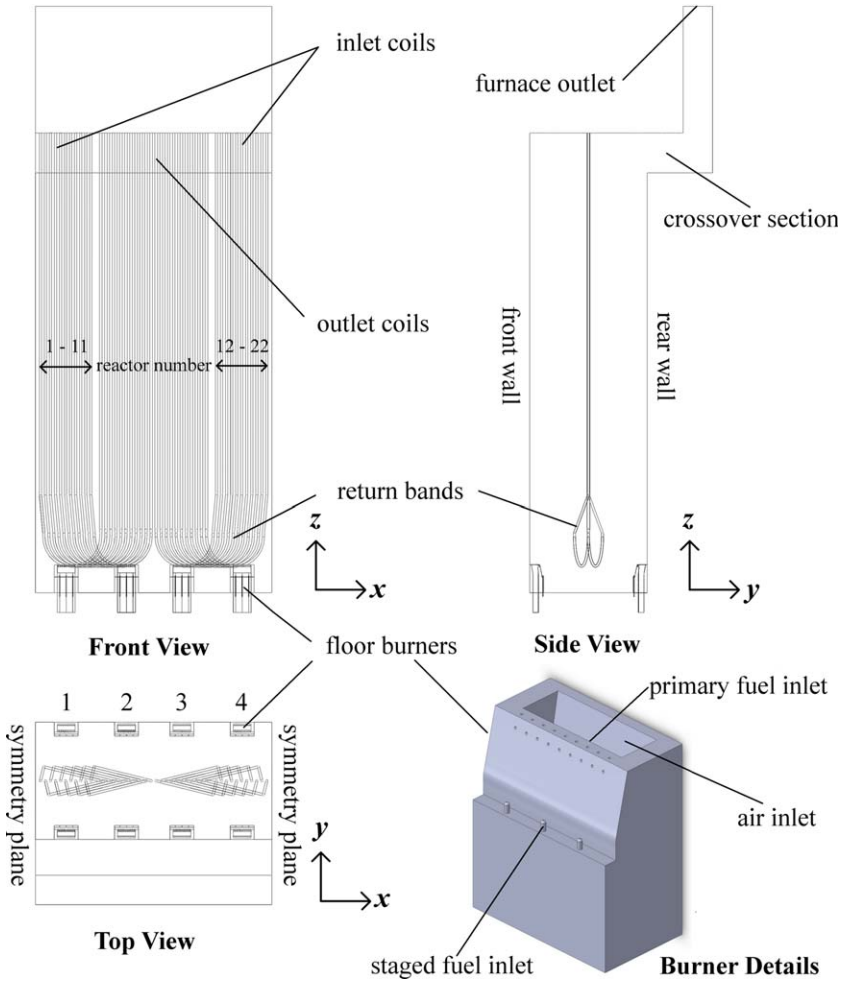

Figure 4. Schematic representation of the simulated furnace segment and detailed burner geometry.

[Color figure can be viewed in the online issue, which is available at wileyonlinelibrary.com.]

using an initial guess for the external Tube Metal Temperature (TMT) profiles as thermal boundary condition on the reactor outer walls. When the residuals of all the transport equations are lower than 10^{-4} (for energy equation is 10^{-6}) and the changes of the flow variables such as stack outlet temperature and O_2 mole fraction over 500 iterations are below 0.1 K and 0.05%, respectively, the simulation is said to be converged. The tube external heat flux q_o which consists of q_{rad} and q_{conv} is then obtained by the models and expressions discussed previously in the turbulence model and the radiation model sections. Afterwards q_o is converted to the heat flux based on the internal tube area, q_i, by the following expression $\frac{q_o}{q_i} = \frac{d_i}{d_o}$. By solving Eqs. 3–5 for each of the 22 reactors, updated external TMT profiles for all reactors are generated. This process is repeated until the maximum differences between the previous and the updated TMTs for every reactors are less than 1 K. All 22 reactors were simulated using updated heat flux profiles obtained from the furnace simulation, whereas in previous coupled simulations[19,20,22,23,62] only one reactor was simulated. The total flow rate was uniformly distributed over all reactors to enable an easy evaluation of the variation in cracking severity over the different reactors due to shadow effects. The industrial unit is also operated with a uniform mass flow rate distribution.

The furnace simulations were performed on two 32-core computing nodes with AMD Magny-Cours Opteron 6136 processors and required about 15 h and 20 h wall time for gray and nongray cases respectively. The CPU time of the reactor simulations is negligible, requiring less than 2 min for 22 reactor simulations. In total 5 furnace-reactor iterations were required for each of the three cases to be converged. It thus takes approximately 75 and 100 h to finish a gray or a nongray case on two 32-core machines respectively, as shown in Table 4. The 4π angular space at each spatial location was discretized into 32 solid angles in DO model to satisfy the radiative heat transfer calculation accuracy, which means the radiative intensities in all 32 solid angles need be stored for every cell for the gray gas simulation. In a nongray simulation, the number increases to 9×32 since the RTE is solved for all 9 bands. This result in very large disk space requirements, that is, about 3.7 and 21.8 GBs for one gray and nongray data file, respectively.

Results and Discussion

Flow variables in the furnace

Three cases were studied: a "gray gas radiation model and detailed burner geometry" case, a "non-gray gas radiation model and detailed burner geometry" case and a "non-gray gas radiation model and simplified burner geometry" case. They are referred to as "gray detailed," "non-gray detailed," and "non-gray simplified," respectively.

As shown in the top view in Figure 4, four burner sets are positioned in the furnace, each consisting of two burners at opposite sides of the reactors. The flue gas velocity profiles

Table 3. Furnace Dimensions and Operating Conditions

Simulated furnace segment	
Length *x*-direction (m)	5.969
Width *y*-direction (m)	2.964
Height *z*-direction (m)	11.609
Number of burners	8
Firing condition	
Fuel gas flow rate (kg/s)	0.2777
Air equivalence ratio	1.2
Fuel gas inlet temperature (K)	288.75
Furnace outlet pressure (Pa)	101300
Fuel composition (mol %)	
CH_4	88.55
H_2	11.14
CO	0.17
C_2H_4	0.14
Reactor coils	
Number of coils	22
Reactor coil length (m)	22.792
Number of passes	2
Inlet leg external diameter (m)	0.566
Inlet leg thickness (m)	0.058
Outlet leg external diameter (m)	0.666
Outlet leg thickness (m)	0.078
Coil operating condition	
Feedstock flow rate of single coil (kg/s)	0.0914
Steam dilution ratio (kg/kg)	0.5
Coil inlet temperature (K)	853.15
Coil inlet pressure (Pa)	236325
Feedstock PIONA (wt %)	
n-Paraffins	29.25
i-Paraffins	29.25
Naphthenes	31.5
Aromatics	10
Material properties	
Furnace refractory emissivity	0.75
Reactor tube skin emissivity	0.85

along the width of the furnace at the *x*-coordinate of the center of the different burner sets for the gray detailed case are depicted in Figure 5. For $z = 1$ m, the velocity difference between the burner sets is less pronounced compared to the profiles at $z = 10$ m. The only exception is at the center of the furnace where burner set 1 and 4 show a higher downward velocity compared to burner set 2 and 3 in Figure 5a. The start of the return bends are located near burner set 1 and 4, creating more space between the reactors for the flue gas to pass. However, near burner set 2 and 3 the end of the returns bends are located, creating very little space between the reactors. This observation explains the velocity difference in the furnace center between the four burner sets. At $z = 10$ m in Figure 5b, the flue gas velocity is higher above burner set 2 and 3. The temperature above these burners is slightly higher compared to burner set 1 and 4 because here the outlet tubes are located which absorb less heat. This higher temperature leads to a lower gas density and resulting higher velocity above these burners. As similar results are

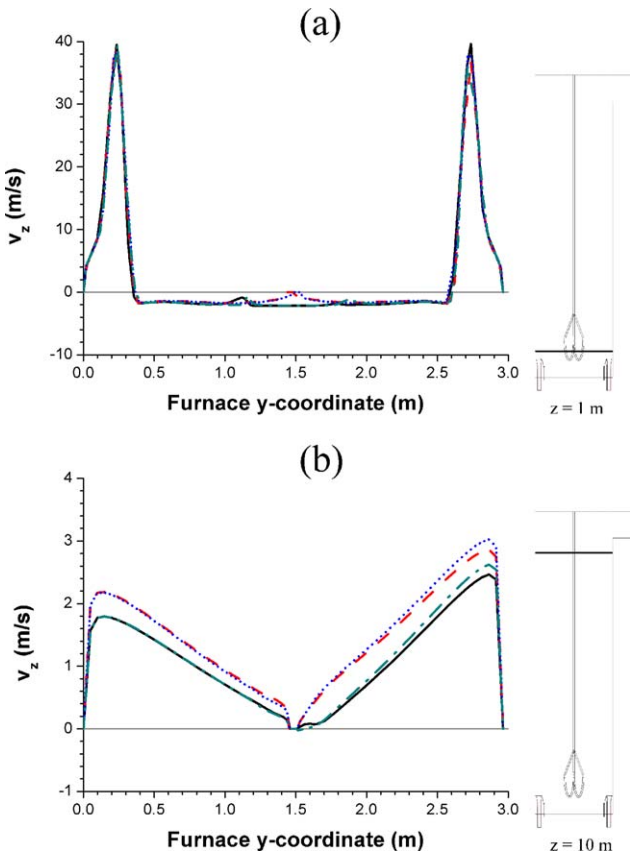

Figure 5. Flue gas velocity *z*-component (m/s) as a function of furnace *y*-coordinate (m) at the center of different burner sets at (a) height = 1 m; (b) height = 10 m: ——— – burner set 1; – – – – burner set 2; ····· – burner set 3; — · — – burner set 4.

[Color figure can be viewed in the online issue, which is available at wileyonlinelibrary.com.]

obtained for the nongray detailed case and the nongray simplified case, comparison between the different cases will be done at the *x*-coordinate of burner set 1, that is, $x = 0.778$ m.

Figure 6 compares the flue gas velocity profiles along the furnace width in the vertical plane $x = 0.778$ m at different heights for the three cases. The gas radiative properties have very limited effect on the flue gas velocity profiles, especially at the lower heights in the furnace. The velocity difference between the gray detailed and nongray detailed cases only becomes distinguishable near the furnace ceiling. Slightly higher velocities are predicted in the nongray detailed case compared to the gray detailed case. The upward velocity is driven by two phenomena: the pressure difference between the burner inlet and the furnace outlet and buoyancy force

Table 4. Comparison of Simulation Results of All Three Cases with the Industrial Design Data

	Gray Detailed	Nongray Detailed	Nongray Simplified	Industrial design data
Flue gas outlet temperature (K)	1298.53	1367.07	1370.39	1364.15
Total heat transfer to the process (kW)	6994.66	6485.71	6453.50	6425
Furnace thermal efficiency (%)	49.41	45.81	45.58	45.48
COT range (K)	1108.68–1205.95	1135.94–1165.01	1136.75–1161.40	1161.15
Ethene yield range (wt %)	30.30–30.71	28.33–29.82	28.43–29.65	28.1
Propene yield range (wt %)	9.28–12.16	13.80–15.93	14.15–15.85	n.a.
P/E ratio range (wt %/wt %)	0.30–0.40	0.46–0.56	0.48–0.56	n.a.
Total clock time on two 32-core machines (*h*)	75.85	96.65	98.90	n.a.

due to temperature differences of the flue gas. The effect of the former is overwhelming at heights near the burners, while the latter starts to have some influence when the effect of the high velocity near the burners has faded out. As higher flue gas temperatures are predicted by the nongray detailed simulation near the furnace top as shown in Figure 7, the upward velocity is higher compared to the gray detailed case. Conversely, the velocity difference between the nongray detailed and nongray simplified simulations is more pronounced as seen in Figure 6. Because of the detailed tip structure of the nozzle, the fuel gas flows out of the burner toward the furnace refractory. This causes a velocity distribution of the nongray detailed case which is narrower and closer to the front and rear wall than that of the nongray simplified case. Higher velocity at the burner outlet leads to stronger recirculation in the furnace as indicated by the higher absolute value of the downward flue gas velocity close to the center of the furnace calculated from the nongray detailed simulation. With the increase of the height near the bottom of the furnace, the velocity predicted by the nongray detailed case decreases rapidly as a result of the friction with the wall. Thus the flue gas velocity for the nongray detailed case is first higher than that of the simplified one and becomes lower at around $z = 4$ m.

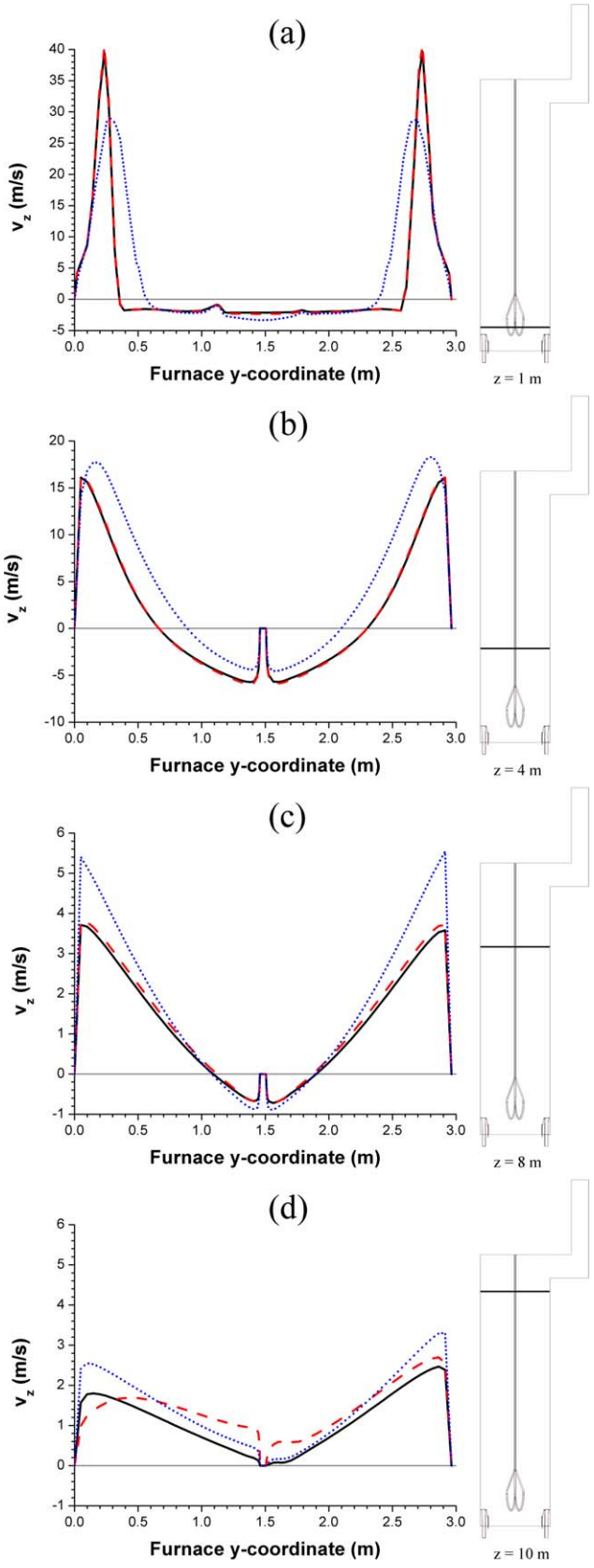

The flue gas temperature contours of a vertical cross section at $x = 0.778$ m are depicted in Figure 7. Higher flame temperatures are simulated when using nongray gas radiative properties, which is consistent with the work of Wang et al.[63] and Stefanidis et al.[27] Although the flue gas temperature differs a lot between the gray detailed and nongray detailed cases, the flame shapes of the two cases are very similar. However, simplification of the burner geometry gives a different temperature distribution with a much wider flame and a shift of the temperature maximum to higher positions. This suggests that the radiative properties mainly determine the mean flue gas temperature while the burner details determine the temperature distribution. Figure 8a shows the mixing-cup averaged flue gas temperature as a function of height. Below 2 m, the burner geometry determines the temperature as the nongray simplified case shows a higher temperature than the gray detailed and nongray detailed cases. The temperature in the nongray simplified case is higher because the fuel and air inlet is lower compared to the detailed cases, that is, at $z = 0$ m instead of at $z = 0.7$ m because of the burner geometry. The influence of the radiative properties is small because only a minor amount of CO_2 and H_2O has been formed at these heights. In the detailed burner cases, fuel is forced toward the air by the burner tip, enhancing turbulent mixing and increasing the consumption rates. This results in a rapid temperature rise in both the detailed burner cases. Above 5 m, the radiative properties determine the temperature as the effect of the burner has faded out and radiation dominates the flue gas temperature instead of reaction and convection.

Figures 9a, b show the mole fraction and consumption rate of methane in the vertical plane at $x = 0.778$ m, respectively. As the feedstock consists of 90 mol % methane, most heat is released from the combustion of CH_4. These two variables are very similar for the two detailed burner simulations, which is in

Figure 6. Flue gas velocity (m/s) as a function of furnace *y*-coordinate (m) at different heights above the center of the burner set 1, that is, at $x = 0.778$ m: (a) height = 1 m; (b) height = 4 m; (c) height = 8 m; (d) height = 10 m: ——— – gray detailed case; – – – – nongray detailed case; ····· – nongray simplified case.

[Color figure can be viewed in the online issue, which is available at wileyonlinelibrary.com.]

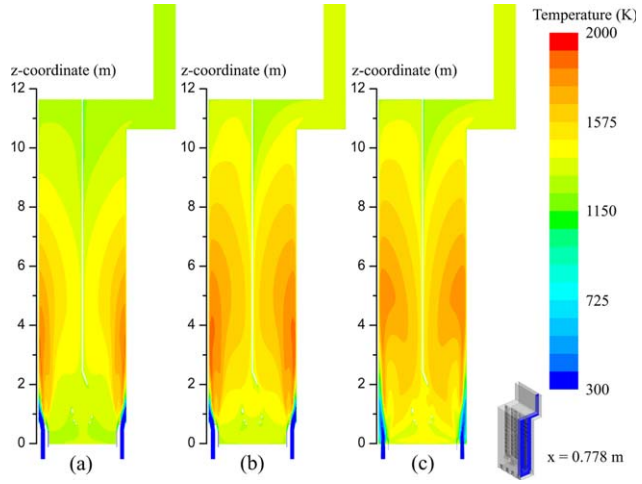

Figure 7. Temperature (K) field in a vertical cross section at the center of the burner set 1, that is, at $x = 0.778$ m: (a) gray detailed case; (b) nongray detailed case; (c) nongray simplified case.

[Color figure can be viewed in the online issue, which is available at wileyonlinelibrary.com.]

agreement with the similar temperatures near the burners of these simulations. Methane flows out of the nozzle in the direction of the refractory wall to better mix with the air, resulting in a narrow flame close to the wall. Two regions with high methane consumption rate corresponding to the primary and staged fuel inlets are observed in Figure 7b. In the nongray simplified case, the primary and staged fuel inlets are both placed in the furnace floor. Hence, the two methane flows meet and a single region with high methane consumption is simulated. As the flame is wider, the average velocity of the flame is lower compared to the detailed burner cases. Less turbulence is therefore created leading to lower consumption rates and a shift upwards of the temperature maximum of about 0.5 m.

Gas radiative properties

The absorption coefficient of the flue gas mixture in the vertical plane $x = 0.778$ is depicted in Figure 10. For the nongray gas cases, the total emissivity is calculated by summing the emissivities of all absorption bands to obtain the absorption coefficient of the flue gas mixture based on Beer's law. The absorption coefficient shows an inverse dependency on temperature, that is, lower values occur at

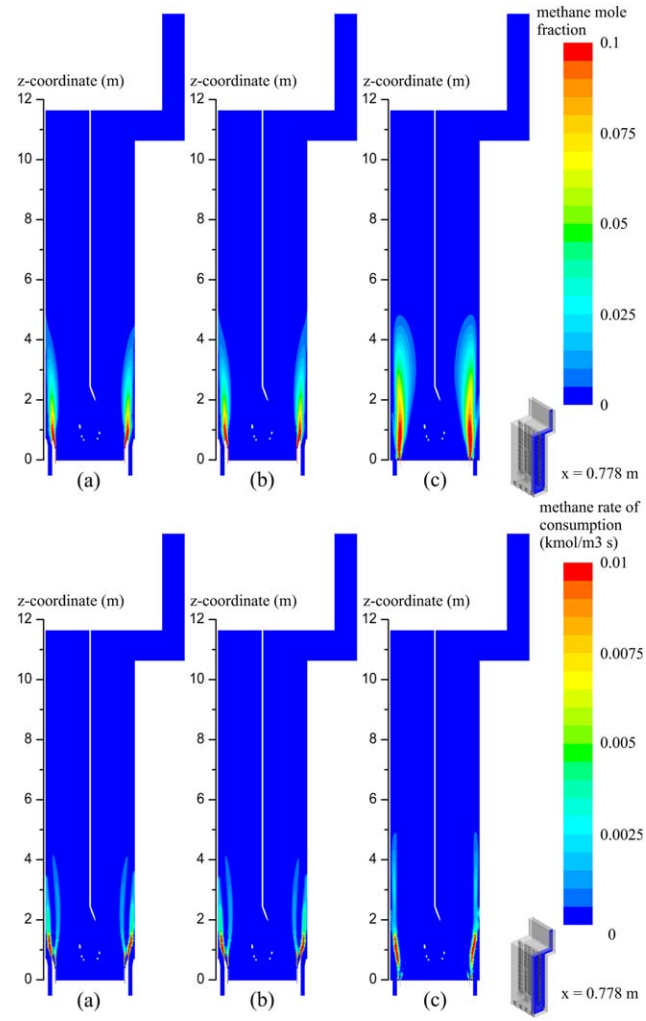

Figure 9. Methane mole fraction (top) and methane rate of consumption (kmol/m^3/s) (bottom) field in a vertical cross section at the center of burner set 1, that is, at $x = 0.778$ m: (a) gray detailed case; (b) nongray detailed case; (c) nongray simplified case.

[Color figure can be viewed in the online issue, which is available at wileyonlinelibrary.com.]

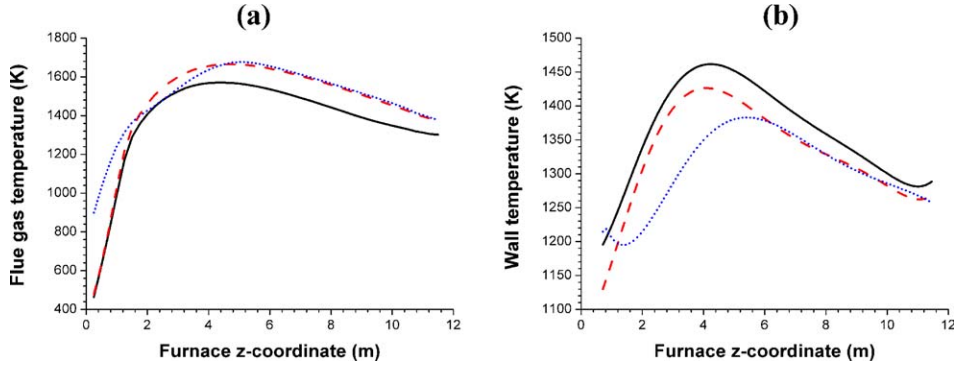

Figure 8. (a) Mixing-cup averaged flue gas temperature (K) and (b) area-averaged furnace refractory wall temperature (K) as a function of furnace *z*-coordinate (m) above the burner at $x = 0.778$ m: ——— – gray detailed case; – – – – nongray detailed case; ····· – nongray simplified case.

[Color figure can be viewed in the online issue, which is available at wileyonlinelibrary.com.]

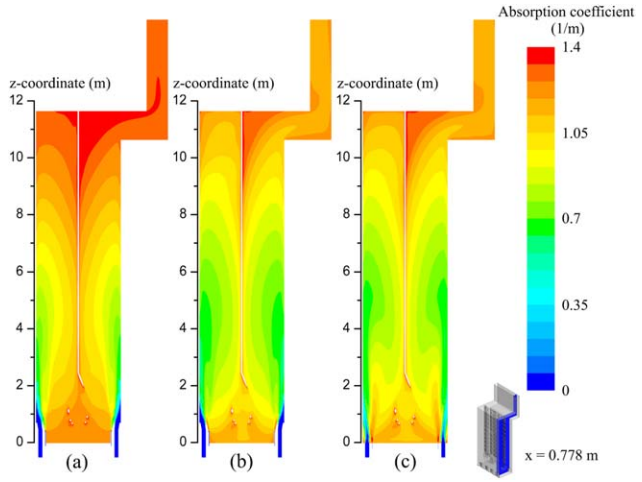

Figure 10. Total absorption coefficient k (1/m) field in a vertical cross section at the center of burner set 1, that is, at $x = 0.778$ m: (a) gray detailed case; (b) nongray detailed case; (c) nongray simplified case.

[Color figure can be viewed in the online issue, which is available at wileyonlinelibrary.com.]

higher temperatures, which is in agreement with Figure 1a at the temperatures prevailing in the furnace. Only near the burner inlets do low temperatures and low absorption coefficients coexist as fuel conversion is low here and no absorbing species, that is, H_2O or CO_2 are present.

It would be expected that the calculated furnace thermal efficiency, that is, the ratio of the heat transferred to the reactors to the total heat release, using a nongray gas radiation model is higher as the flame temperature is higher, which means more heat is emitted from the flame. However, the opposite is observed. The bands in a nongray model can be divided into two main band categories: the spectral windows and the absorbing/emitting bands. Radiation emitted by the refractory walls with wavelengths in the spectral windows travel directly to the reactor coils without interference

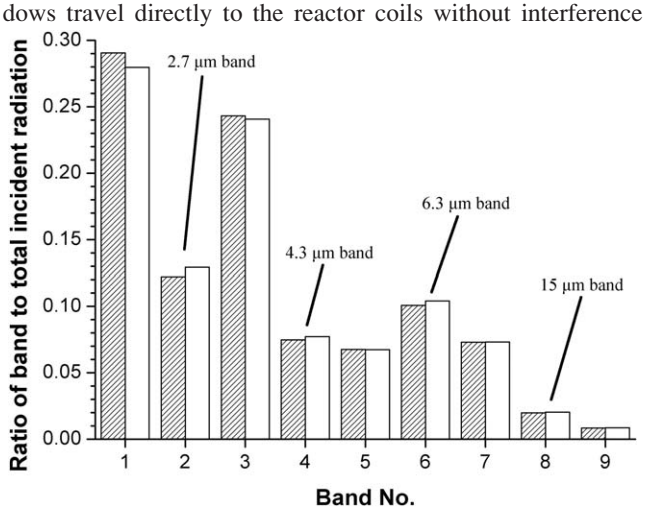

Figure 11. The ratio of the band incident radiation to the total incident radiation on the reactors: ▨ – nongray detailed case; ▭ – nongray simplified case where band 2, 4, 6, and 8 represent the 2.7, 4.3, 6.3, and 15 μm absorption bands, respectively and band 1, 3, 5, 7, and 9 represent the spectral windows.

of the flue gas. Radiation with wavelengths in the other bands experiences an absorbing and re-emitting process by the flue gas before reaching the reactors. Figure 11 shows the contribution of the nine bands to the total incident radiation on the reactors for the nongray detailed and nongray simplified cases. As very similar results are obtained for the two cases, only the nongray detailed case is discussed here. About 68% of the total incident radiation on the reactor coils is emitted through the spectral windows, that is, summation over bands 1, 3, 5, 7, and 9 in Figure 11. As in the spectral windows, radiation is determined by the walls, the incident radiation on the reactors depends much more on the refractory wall temperature than on the flue gas temperature, giving rise to a higher furnace thermal efficiency in the gray detailed case due to its higher refractory wall temperature.

Figure 12 shows the band incident radiation in the first spectral window, in the 2.7 μm band and the incident radiation over the entire spectrum for the nongray detailed case in the

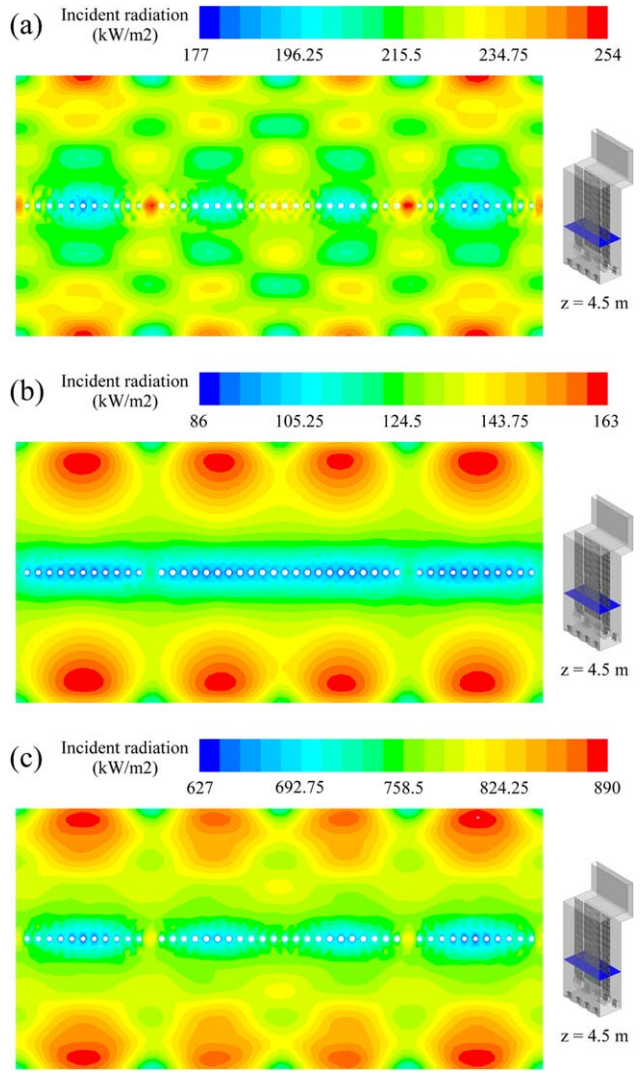

Figure 12. Incident radiation (kW/m^2) field for the nongray detailed case in a horizontal plane at $z = 4.5$ m in the: (a) first spectral window (band 1); (b) 2.7 μm band (band 2); and (c) entire spectrum.

[Color figure can be viewed in the online issue, which is available at wileyonlinelibrary.com.]

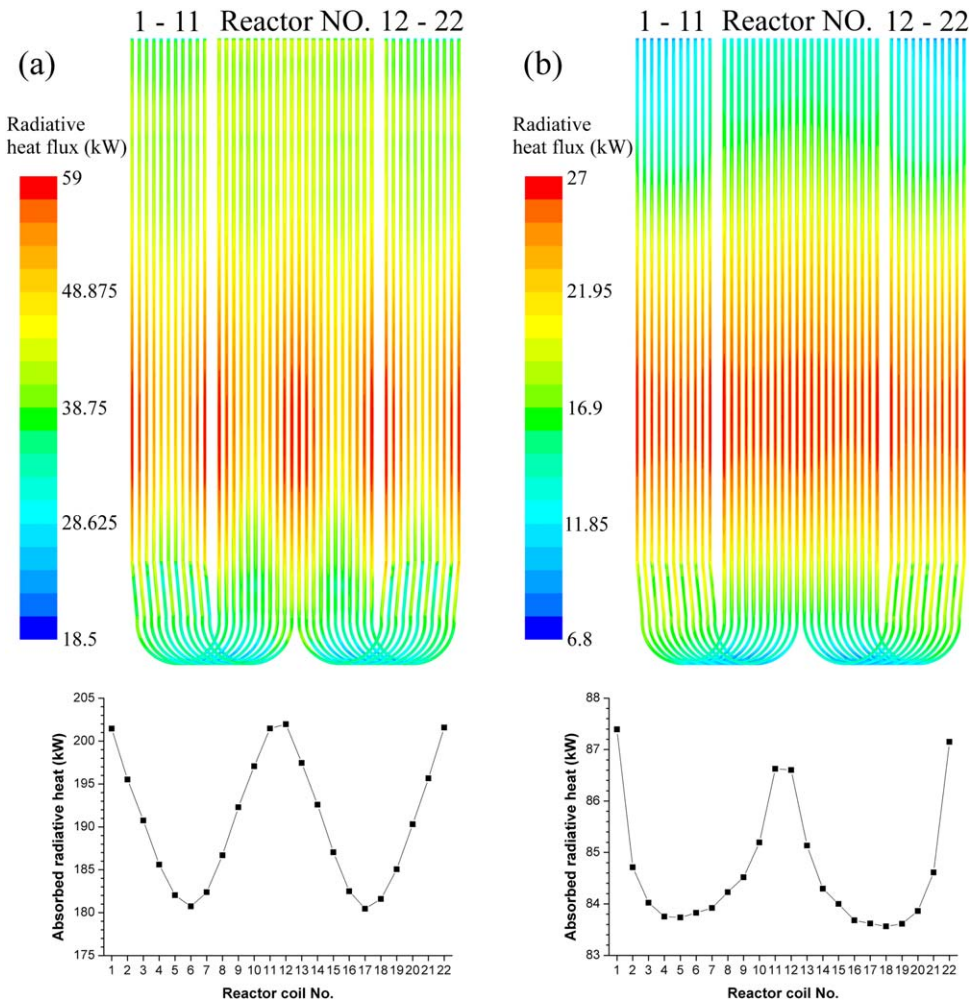

Figure 13. Radiative heat flux (kW) (top) and absorbed radiative heat (kW) (bottom) of all 22 reactors in the: (a) first spectral window (band 1); (b) 2.7 μm band (band 2).

[Color figure can be viewed in the online issue, which is available at wileyonlinelibrary.com.]

horizontal plane $z = 4.5$ m. These bands are chosen as they contribute the most to the total incident radiation of all bands in their band category. The incident radiation of the other bands is very similar to that of the depicted band of their band category. In the spectral window, the incident radiation is determined by the wall and reactor outer wall temperature and the relative position of the surfaces to one another, that is, the view factors. In Figure 12a, the maximum radiation intensity is located just above the burners because the wall temperature is maximal at this height. The reactor tubes in-between two burners receive most radiation in the spectral windows, while the reactors in front of a burner receive the least amount of incident radiation. The configuration of the burners and reactors in the furnace makes that the view factor from the high temperature wall zones, that is, above the burners, is higher to the reactor tubes in-between two burners. A completely different incident radiation distribution is observed for the 2.7 μm absorption band, where the maximum is found about 0.2 m away from the refractory and the incident radiation over the different reactor tubes is more uniform. The latter indicates that the radiation emitted from the refractory is absorbed and redistributed by the flue gas. The change in radiative intensity when it travels through the flue gas is determined by the flue gas absorption coefficient and the temperature as seen in Eqs. (24) and (25). However, the emitted radiation intensity is proportional to the fourth power of the flue gas temperature, while the absorbed radiation intensity, which is proportional to the flue gas absorption coefficient, decreases almost linearly with the temperature in the range of 1000–1900 K. Hence, a large amount of the intensity emitted by the high temperature flame flue gas and furnace refractory walls is absorbed by the flue gas at lower temperature near the reactor coils. This results in a more uniform flue gas temperature and incident radiation. The total incident radiation distribution depicted in Figure 12c is a combination of the incident radiation of the spectral windows and the absorption bands.

Shadow effects and reactor simulations

As a reactor simulation is performed for all 22 reactors individually, the variation of heat transfer to the different reactors and the resulting distribution of Coil Outlet Temperatures (COT) can be studied. Figure 13 shows the radiative heat flux and the absorbed radiative heat of all the reactor coils within the first spectral window and the 2.7 μm band, where the absorbed radiative heat is defined as the integration of the radiative heat flux absorbed by the reactor over the entire coil surface. Similar results as for the incident radiation are seen, that is, the radiative heat flux distribution is more uniform for the absorption band than for the spectral window.

Figure 14 shows the transferred thermal power by radiation and convection, COT, maximum TMT, and propene-to-

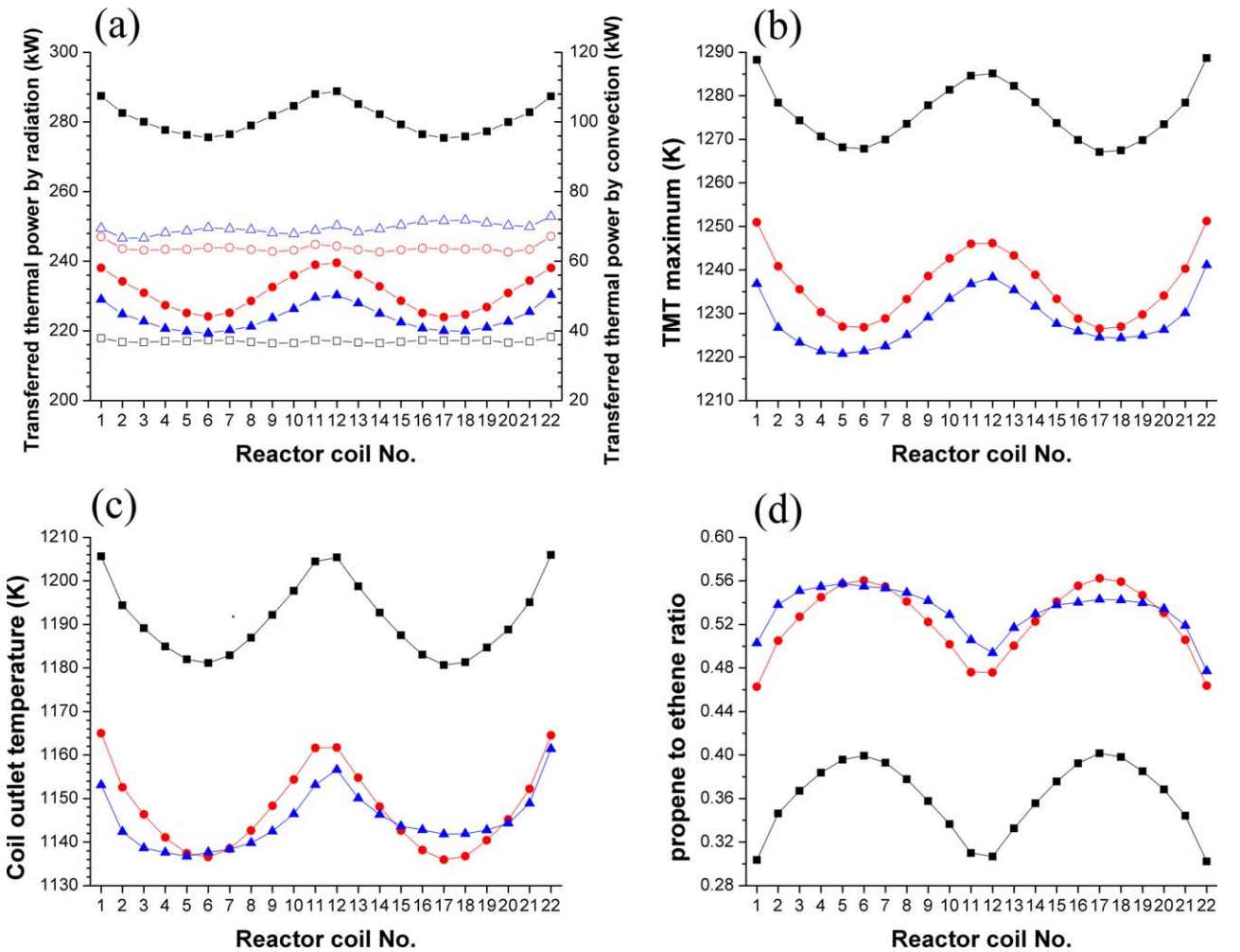

Figure 14. The distribution of (a) transferred thermal power by radiation (solid symbols) and by convection (open symbols) (kW), (b) maximum external TMT (K), (c) COT (K), and (d) propene-to-ethene ratio (wt %/wt %) over all 22 reactors: —■— —□— – gray detailed case; —●— —○— – nongray detailed case; —▲— —△— – nongray simplified case.

[Color figure can be viewed in the online issue, which is available at wileyonlinelibrary.com.]

ethene (P/E) ratio of the different reactors. It is clearly observed from Figure 14a that in all three cases, radiation plays a more important role in the variation of the total transferred thermal power to the reactors than convection. For the gray gas case a lower contribution of convective heat transfer to the reactors is observed. This can be attributed to the lower flue gas temperature near the tube wall for the gray gas simulation. A similar average value of the sum of transferred thermal power by radiation and convection of the two nongray cases suggests that the thermal efficiency of these two cases is almost the same. The average heat transfer predicted in the gray detailed simulation is higher compared to the nongray cases, while the profile shape is very similar to the nongray detailed case. The radiation properties strongly affect the flue gas and wall average temperature, as shown previously in Figure 8. Hence, it mainly determines the average heat transfer to the reactors. Conversely, the burner details mainly affect the temperature distribution in the furnace as shown previously in Figure 7. Accordingly, the burner details determine the distribution of heat transfer over the reactors. The TMT maximum, COTs, and P/E ratios depicted in Figure 14 are a direct consequence of the heat transfer. The average COT and P/E ratio in the gray detailed simulation differs about 45 K and 0.16 from than the nongray detailed simulation values. Accounting for the nongray character of the flue gas mixture is therefore necessary to perform reliable reactor simulations. The maximum COT difference between the reactors is 25.2, 29.1, and 24.6 K for the gray detailed, nongray detailed and nongray simplified case, respectively. A reduction of the nonuniformity of the heat transfer to the reactors could be obtained by, for example, altering the distribution of the fuel over the different burners or the mass flow rate over the different reactors. The TMT maximum for the nongray simplified case are lower than those of the nongray detailed case in spite of the higher thermal power received by some reactors in the simplified burner case. For example reactors 16–19 receive more thermal power in the simplified burner case compared to the nongray detailed case but their TMTs are lower. This is a result of the more uniform heat flux along the reactor axial coordinate in the simplified burner case as shown in Figure 15a. Hence, to perform run-length predictions the effect of burner details on the heat flux profile should be taken into account.

Figure 15 shows the heat flux, TMT, process gas temperature and ethene and propene yield profiles as a function of axial position for reactor 1. Clearly, the nongray simplified case simulates a more uniform heat flux profile than the nongray detailed case, resulting in a lower TMT maximum. The

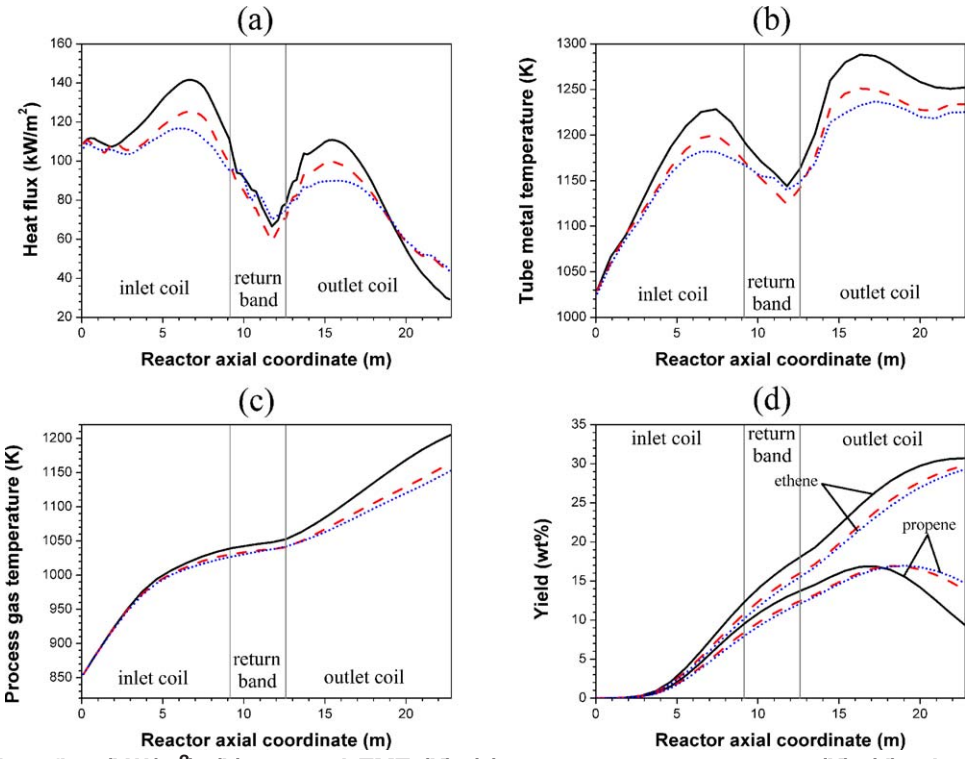

Figure 15. (a) Heat flux (kW/m^2); (b) external TMT (K); (c) process gas temperature (K); (d) ethene and propene yields (wt %) as a function of the reactor axial coordinate (*m*) for reactor 1: ——— – gray detailed case; – – – – nongray detailed case; ····· – nongray simplified case.

[Color figure can be viewed in the online issue, which is available at wileyonlinelibrary.com.]

heat flux, TMT and process gas temperature are greatly overpredicted by the gray gas radiation model, leading to an overprediction of the propene consumption near the reactor outlet.

Finally, in Table 4 the results of the three cases are compared to industrial design data. The heat transfer to the reactors when using a nongray gas model is about 500 kW lower compared to the gray gas case and quite close to the industrial design data. Consequently, the thermal efficiency and flue gas outlet temperature are also in good agreement with the industrial data. The necessity of using a nongray gas radiation model to accurately predict the heat transfer process in the cracking furnace is evident from these results. As the nongray detailed and nongray simplified burner cases give similar results in terms of total transferred thermal power and thermal efficiency, it is reasonable to omit the detailed burner geometry to reduce meshing effort for some industrial applications where only the total transferred heat and thermal efficiency are of interest. However, the shape of the heat flux profile to the reactors can be substantially different when using a simplified burner geometry, and hence, the resulting TMT's and runlength of the furnace are unreliable when using simplified burner geometries. The COT and olefin yields differ significantly between the different cases and the industrial data. Measuring the COT for all reactors in a furnace accurately remains one of the challenges of the industry.[64] Moreover, the use of a detailed single-event microkinetic model that has been validated over a broad range of conditions is essential to predict accurately the product yields.[35]

Conclusions

Fully coupled simulations of an industrial steam cracking furnace equipped with floor burners are performed and the influences of flue gas radiative properties, burner geometry and shadow effects are evaluated. A nongray gas radiation model which takes four main H_2O and CO_2 absorption bands into account is developed from the EWBM. The WSGGM embodied in FLUENT is used as gray gas radiation model. The simulation shows that the gray gas radiation model underpredicts the flue gas outlet temperature by about 70 K compared to the nongray gas radiation model, resulting in a 3.6% higher thermal efficiency. This is quite significant as it results in a 44 K higher average COT. The nongray gas radiation model provides much better results for the radiative heat transfer in the furnace with flue gas outlet temperature and thermal efficiency very close to the industrial design data. Similar total transferred thermal power are obtained in the nongray detailed and nongray simplified burner cases. However, the shape of the heat flux profile to the individual reactors can be substantially different when using a simplified burner geometry. Shadow effects further complicate interpretation. For the USC furnace simulated in this work shadow effects cause a maximum difference in COT of 29 K and a difference in propene-over-ethene of 0.1 between two different U-coils in the furnace. To obtain more uniform COTs and olefin yields for the individual reactors, the cracking feedstock could be unevenly distributed over the latter. During the design of a new unit, a combination of floor and wall burners could further improve the heat flux uniformity to the reactors. As wall burners can be regulated separately, they can make up for the nonuniformities induced by the floor burners.

Acknowledgments

This work was carried out using the STEVIN Supercomputer Infrastructure at Ghent University, funded by Ghent

University, the Flemish Supercomputer Center (VSC), the Hercules Foundation and the Flemish Government—Department EWI. The financial support from the BOF Bilateral Scientific Cooperation (ECUST/LCT), the Long Term Structural Methusalem Funding by the Flemish Government, and the China Scholarship Council (CSC) are acknowledged. This work is supported by Major State Basic Research Development Program of China (2012CB720500), National Natural Science Foundation of China (U1162202), Shanghai R&D Platform Construction Program (13DZ2295300) and the 111 Project (B08021). CMS acknowledges financial support from a doctoral fellowship from the Fund for Scientific Research Flanders (FWO).

Notation

Roman

A = surface area, m^2
A = eddy dissipation model constant, A=4.0, -
A = band absorptance, m^{-1}
ANN = artificial neutral network, -
A^* = dimensionless band absorptance, -
a_i = weight factor of fictitious gray gas i, -
B = eddy dissipation model constant, B=0.5, -
b = EWBM pressure parameter, -
$b_{i,j}$ = temperature coefficient, -
c_p = heat capacity, J/mol/K
C = species concentration, mol/m^3
CFD = computational fluid dynamics, -
COT = coil outlet temperature, -
C_2 = constant for Planck function, $C_2=1.4388\times10^{-2}$, m·K
$C_{1\varepsilon}$ = RNG k-ε model constant, $C_{1\varepsilon}$=1.42, -
$C_{2\varepsilon}$ = RNG k-ε model constant, $C_{2\varepsilon}$=1.68, -
C_μ = RNG k-ε model constant, C_μ=0.0845, -
DO = discrete ordinate, -
d_i = inner diameter of reactor coil, m
d_o = outer diameter of reactor coil, m
E = specific total energy, J/kg
EDM = eddy-dissipation model, -
EWBM = exponential wide band model, -
F = mole flow rate, mol/s
f = Fanning friction factor, -
$f(n\lambda T)$ = fractional emissive power, -
g = gravitational acceleration, m/s^2
h_c = convective heat transfer coefficient, $W/m^2\cdot K$
h_i = specific enthalpy of species i, J/mol
ΔH = heat of reaction, J/mol
I = radiation intensity, W/m^2
$\vec{J}_i$ = diffusion flux of species i, $mol/m^2\cdot s$
k = turbulent kinetic energy, m^2/s^2
k_p = turbulent kinetic energy of the first near-wall node P, m^2/s^2
k_{eff} = effective conductivity,
L = path length, m
LBLRTM = line-by-line radiative transfer model, -
M_w = molecular weight, kg/mol
N_s = total number of species, -
N_R = total number of reactions, -
n = refractive index, -
n = EWBM pressure parameter, -
$\vec{n}$ = normal pointing out of the domain, -
p = total pressure, Pa
q = heat flux, W/m^2
q_{conv} = convective heat flux, W/m^2
q_i = tube internal heat flux, W/m^2
q_{in} = incident radiative heat flux on a wall, W/m^2
q_o = tube external heat flux, W/m^2
q_{out} = radiative heat flux leaving a wall, W/m^2
q_{rad} = radiative heat flux, W/m^2
R = ideal gas constant, R=8.3145, J/mol·K
R_i = net production rate of species i, $mol/m^3\cdot s$
RANS = Reynolds averaged Navier Stokes, -
RNG = renormalization group, -
RTE = radiative transfer equation, -
r = intrinsic reaction rate, $mol/m^3\cdot s$
$\vec{r}$ = position vector, -
r_b = radius of the bend, -
SIMPLE = semi-implicit method for pressure-linked equations, -
S_E = energy source term, $J/m^3\cdot s$
S_M = momentum source term, $kg/m^2\cdot s^2$
$\vec{s}$ = unit direction vector, -
$\vec{s}'$ = scattering direction vector, -
T = temperature, K
T_p = temperature of the first near-wall node P, K
$T_{w,i}$ = internal tube metal temperature, K
$T_{w,o}$ = external tube metal temperature, K
T^* = dimensionless temperature, -
TMT = external tube metal temperature, K
UDF = user defined function, -
USC = ultraselective conversion, -
$\vec{u}$ = velocity, m/s
WSGGM = weighted sum of gray gas model, -
V = volume, m^3
V_m = molar volume, m^3/mol
X = density path length, kg/m^2
Y_i = mole fraction of species i, mol/mol
Y_P = mole fraction of any product species P, mol/mol
Y_R = mole fraction of a particular reactant R, mol/mol
y_p = distance from the wall to the first near-wall node P, m
y^* = dimensionless distance from the wall, -

Greek

α = band strength parameter, $m^{-1}/kg\cdot m^{-2}$
α_0 = EWBM correlation parameter, $m^{-1}/kg\cdot m^{-2}$
α_k = RNG k-ε model constant, α_k=1.393, -
α_ε = RNG k-ε model constant, α_ε=1.393, -
β = RNG k-ε model constant, β=0.012, -
β = line overlapping parameter, -
β_0^* = EWBM correlation parameter, -
ε = turbulent dissipation rate, m^2/s^3
ε = emissivity, -
ζ = Nekrasov factor for bends, -
η = wavenumber, cm^{-1}
η_0 = RNG k-ε model constant, η_0=4.38, -
κ = absorption coefficient, m^{-1}
λ = wavelength, μm
λ_w = thermal conductivity of tube metal, W/m·K
μ = viscosity, Pa·s
$\nu'_{R,j}$ = stoichiometric coefficient for reactant R in reaction j, -
$\nu_{P,j}$ = stoichiometric coefficient for product P in reaction j, -
ρ = density, kg/m^3
σ = Stefan-Boltzmann constant, $\sigma=5.67\times10^{-8}$, $W/m^2\cdot K^4$
σ_s = scattering coefficient, m^{-1}
τ_0 = optical thickness at the band center, -
$\bar{\bar{\tau}}$ = stress tensor, Pa
Φ = scattering phase function, -
Ω = solid angle, sr
ω = band width parameter, m^{-1}
ω_0 = EWBM correlation parameter, m^{-1}

Subscript

b = black body, -
l = lower, -
t = turbulent, -
u = upper,-
w = wall, -
λ = spectral, -

Literature Cited

1. Ren T, Patel M, Blok K. Olefins from conventional and heavy feedstocks: energy use in steam cracking and alternative processes. *Energy*. 2006;31(4):425–451.
2. Van Geem KM, Reyniers M-F, Marin GB, Song J, Green WH, Matheu DM. Automatic reaction network generation using RMG for steam cracking of n-hexane. *AIChE J*. 2006;52(2):718–730.
3. Sun W, Saeys M. Construction of an ab initio kinetic model for industrial ethane pyrolysis. *AIChE J*. 2011;57(9):2458–2471.

4. Sabbe MK, Van Geem KM, Reyniers M-F, Marin GB. First principle-based simulation of ethane steam cracking. *AIChE J*. 2011; 57(2):482–496.
5. Ranzi E, Frassoldati A, Granata S, Faravelli T. Wide-range kinetic modeling study of the pyrolysis, partial oxidation, and combustion of heavy n-alkanes. *Ind Eng Chem Res*. 2004;44(14):5170–5183.
6. Schietekat CM, Van Cauwenberge DJ, Van Geem KM, Marin GB. Computational fluid dynamics-based design of finned steam cracking reactors. *AIChE J*. 2014;60(2):794–808.
7. Van Geem KM, Žajdlík R, Reyniers M-F, Marin GB. Dimensional analysis for scaling up and down steam cracking coils. *Chem Eng J*. 2007;134(1–3):3–10.
8. Van Geem KM, Heynderickx GJ, Marin GB. Effect of radial temperature profiles on yields in steam cracking. *AIChE J*. 2004;50(1):173–183.
9. Berreni M, Wang M. Modelling and dynamic optimization of thermal cracking of propane for ethylene manufacturing. *Comput Chem Eng*. 2011;35(12):2876–2885.
10. Sadrameli SM, Green AES. Systematics and modeling representations of naphtha thermal cracking for olefin production. *J Anal Appl Pyrolysis*. 2005;73(2):305–313.
11. Heynderickx GJ, Froment GF. Simulation and comparison of the run length of an ethane cracking furnace with reactor tubes of circular and elliptical cross sections. *Ind Eng Chem Res*. 1998;37(3):914–922.
12. Plehiers PM, Reyniers GC, Froment GF. Simulation of the run length of an ethane cracking furnace. *Ind Eng Chem Res*. 1990; 29(4):636–641.
13. Hottel HC, Sarofim AF. *Radiative Transfer*. New York: McGraw-Hill, 1967.
14. Oprins AJM, Heynderickx GJ, Marin GB. Three-dimensional asymmetric flow and temperature fields in cracking furnaces. *Ind Eng Chem Res*. 2001;40(23):5087–5094.
15. Heynderickx GJ, Oprins AJM, Marin GB, Dick E. Three-dimensional flow patterns in cracking furnaces with long-flame burners. *AIChE J*. 2001;47(2):388–400.
16. Oprins AJM, Heynderickx GJ. Calculation of three-dimensional flow and pressure fields in cracking furnaces. *Chem Eng Sci*. 2003;58(21): 4883–4893.
17. Stefanidis GD, Merci B, Heynderickx GJ, Marin GB. CFD simulations of steam cracking furnaces using detailed combustion mechanisms. *Comput Chem Eng*. 2006;30(4):635–649.
18. Habibi A, Merci B, Heynderickx GJ. Impact of radiation models in CFD simulations of steam cracking furnaces. *Comput Chem Eng*. 2007;31(11):1389–1406.
19. Hu G, Wang H, Qian F, Zhang Y, Li J, Van Geem KM, Marin GB. Comprehensive CFD simulation of product yields and coking rates for a floor- and wall-fired naphtha cracking furnace. *Ind Eng Chem Res*. 2011;50(24):13672–13685.
20. Hu G, Wang H, Qian F, Van Geem KM, Schietekat CM, Marin GB. Coupled simulation of an industrial naphtha cracking furnace equipped with long-flame and radiation burners. *Comput Chem Eng*. 2012;38:24–34.
21. Stefanidis GD, Van Geem KM, Heynderickx GJ, Marin GB. Evaluation of high-emissivity coatings in steam cracking furnaces using a non-grey gas radiation model. *Chem Eng J*. 2008;137(2):411–421.
22. Lan X, Gao J, Xu C, Zhang H. Numerical simulation of transfer and reaction processes in ethylene furnaces. *Chem Eng Res Des*. 2007; 85(12):1565–1579.
23. Guihua H, Honggang W, Feng Q. Numerical simulation on flow, combustion and heat transfer of ethylene cracking furnaces. *Chem Eng Sci*. 2011;66(8):1600–1611.
24. Coelho PJ. Numerical simulation of radiative heat transfer from non-gray gases in three-dimensional enclosures. *J Quant Spectrosc Radiat Transf*. 2002;74(3):307–328.
25. Modest MF. The treatment of nongray properties in radiative heat transfer: from past to present. *J Heat Transfer*. 2013;135(6):061801–061801.
26. Heynderickx GJ, Nozawa M. Banded gas and nongray surface radiation models for high-emissivity coatings. *AIChE J*. 2005;51(10): 2721–2736.
27. Stefanidis GD, Merci B, Heynderickx GJ, Marin GB. Gray/nongray gas radiation modeling in steam cracker CFD calculations. *AIChE J*. 2007;53(7):1658–1669.
28. Heynderickx GJ, Cornelis GG, Froment GF. Circumferential tube skin temperature profiles in thermal cracking coils. *AIChE J*. 1992; 38(12):1905–1912.
29. Stefanidis GD, Heynderickx GJ, Marin GB. Development of reduced combustion mechanisms for premixed flame modeling in steam cracking furnaces with emphasis on NO emission. *Energy Fuels*. 2006;20(1):103–113.
30. Bilger RW, Stårner SH, Kee RJ. On reduced mechanisms for methane-air combustion in nonpremixed flames. *Combust Flame*. 1990;80(2):135–149.
31. Stagni A, Cuoci A, Frassoldati A, Faravelli T, Ranzi E. A fully coupled, parallel approach for the post-processing of CFD data through reactor network analysis. *Comput Chem Eng*. 2014;60:197–212.
32. Habibi A, Merci B, Heynderickx GJ. Multiscale modeling of turbulent combustion and NOx emission in steam crackers. *AIChE J*. 2007;53(9):2384–2398.
33. Cuoci A, Frassoldati A, Stagni A, Faravelli T, Ranzi E, Buzzi-Ferraris G. Numerical modeling of NOx formation in turbulent flames using a kinetic post-processing technique. *Energy Fuels*. 2012;27(2):1104–1122.
34. Hassan G, Pourkashanian M, Ingham D, Ma L, Newman P, Odedra A. Predictions of CO and NOx emissions from steam cracking furnaces using GRI2.11 detailed reaction mechanism—A CFD investigation. *Comput Chem Eng*. 2013;58:68–83.
35. Van Geem KM, Reyniers MF, Marin GB. Challenges of modeling steam cracking of heavy feedstocks. *Oil Gas Sci Technol—Rev IFP*. 2008;63(1):79–94.
36. Pyl SP, Van Geem KM, Reyniers M-F, Marin GB. Molecular reconstruction of complex hydrocarbon mixtures: an application of principal component analysis. *AIChE J*. 2010;56(12):3174–3188.
37. Van Geem KM, Hudebine D, Reyniers MF, Wahl F, Verstraete JJ, Marin GB. Molecular reconstruction of naphtha steam cracking feedstocks based on commercial indices. *Comput Chem Eng*. 2007;31(9): 1020–1034.
38. Versteeg HK, Malalasekera W. An Introduction to Computational Fluid Dynamics: The Finite Volume Method. Harlow: Longman Group Ltd, 1995.
39. Yakhot V, Orszag SA, Thangam S, Gatski TB, Speziale CG. Development of turbulence models for shear flows by a double expansion technique. *Phys Fluids A: Fluid Dyn* (1989–1993). 1992;4(7):1510–1520.
40. Launder BE, Spalding DB. The numerical computation of turbulent flows. *Comput Methods Appl Mech Eng*. 1974;3(2):269–289.
41. ANSYS, Inc. *ANSYS FLUENT User's Guide, Release 14.0*. ANSYS, Inc, 2011.
42. Westbrook CK, Dryer FL. Simplified reaction mechanisms for the oxidation of hydrocarbon fuels in flames. *Combust Sci Technol*. 1981;27(1–2):31–43.
43. Magnussen BF, Hjertager BH. On mathematical modeling of turbulent combustion with special emphasis on soot formation and combustion. *Symp (Int) Combust*. 1977;16(1):719–729.
44. Yeoh GH, Yuen KK. *Computational Fluid Dynamics in Fire Engineering: Theory, Modelling and Practice*. Burlington: Butterworth-Heinemann, 2009.
45. Chui EH, Raithby GD. Computation of radiant heat transfer on a non-orthogonal mesh using the finite-volume method. *Numer Heat Transfer, Part B: Fundam*. 1993;23(3):269–288.
46. Murthy JY, Mathur SR. Finite volume method for radiative heat transfer using unstructured meshes. *J Thermophys Heat Transfer*. 1998;12(3):313–321.
47. Baukal CE, Gershtein V, Li XJ. *Computational Fluid Dynamics in Industrial Combustion*. Boca Raton: CRC Press, 2000.
48. Rothman LS, Gordon IE, Barber RJ, Dothe H, Gamache RR, Goldman A, Perevalov VI, Tashkun SA, Tennyson J. HITEMP, the high-temperature molecular spectroscopic database. *J Quant Spectrosc Radiat Transfer*. 2010;111(15):2139–2150.
49. Rothman LS, Gordon IE, Barbe A, Benner DC, Bernath PF, Birk M, Boudon V, Brown LR, Campargue A, Champion JP, Chance K, Coudert LH, Dana V, Devi VM, Fally S, Flaud JM, Gamache RR, Goldman A, Jacquemart D, Kleiner I, Lacome N, Lafferty WJ, Mandin JY, Massie ST, Mikhailenko SN, Miller CE, Moazzen-Ahmadi N, Naumenko OV, Nikitin AV, Orphal J, Perevalov VI, Perrin A, Predoi-Cross A, Rinsland CP, Rotger M, Šimečková M, Smith MAH, Sung K, Tashkun SA, Tennyson J, Toth RA, Vandaele AC, Vander Auwera J. The HITRAN 2008 molecular spectroscopic database. *J Quant Spectrosc Radiat Transfer*. 2009;110(9–10):533–572.
50. Modest MF. *Radiative Heat Transfer*, 3rd ed. Boston: Academic Press, 2013.
51. Grosshandler WL. *RADCAL: A Narrow-Band Model for Radiation Calculations in a Combustion Environment*. National Institute of Standards and Technology, 1993.

52. Soufiani A, Taine J. High temperature gas radiative property parameters of statistical narrow-band model for H2O, CO2 and CO, and correlated-K model for H2O and CO2. *Int J Heat Mass Transfer*. 1997;40(4):987–991.
53. Edwards DK, Balakrishnan A. Thermal radiation by combustion gases. *Int J Heat Mass Transfer*. 1973;16(1):25–40.
54. Smith TF, Shen ZF, Friedman JN. Evaluation of coefficients for the weighted sum of gray gases model. *J Heat Transfer*. 1982;104(4): 602–608.
55. Coppalle A, Vervisch P. The total emissivities of high-temperature flames. *Combust Flame*. 1983;49(1–3):101–108.
56. Edwards DK, Matavosian R. Scaling rules for total absorptivity and emissivity of gases. *J Heat Transfer*. 1984;106(4):684–689.
57. Lallemant N, Weber R. A computationally efficient procedure for calculating gas radiative properties using the exponential wide band model. *Int J Heat Mass Transfer*. 1996;39(15):3273–3286.
58. Edwards DK. Molecular gas band radiation. In: Thomas FI, James PH, editors. *Advances in Heat Transfer*, Vol. 12. Elsevier, 1976: 115–193.
59. Ströhle J, Coelho PJ. On the application of the exponential wide band model to the calculation of radiative heat transfer in one- and two-dimensional enclosures. *Int J Heat Mass Transfer*. 2002;45(10): 2129–2139.
60. Brewster Q. *Thermal Radiative Transfer and Properties*. New York: Wiley, 1992.
61. Leckner B. Spectral and total emissivity of water vapor and carbon dioxide. *Combust Flame*. 1972;19(1):33–48.
62. Han YL, Xiao R, Zhang MY. Combustion and pyrolysis reactions in a naphtha cracking furnace. *Chem Eng Technol*. 2007;30(1):112–120.
63. Wang L, Modest MF, Haworth DC, Turns SR. Modelling nongrey gas-phase and soot radiation in luminous turbulent nonpremixed jet flames. *Combust Theory Model*. 2005;9(3):479–498.
64. Brown DJ, Cremer MA, Smith PJ, Waibel RT. Fireside modeling in cracking furnaces. In: Proceedings of 9th Ethylene Producers' Conference, Vol. 6. New York: American Institute of Chemical Engineers, 1997:158–193.

Manuscript received Sep. 11, 2014, and revision received Nov. 13, 2014.